Hydrogen-Bonding 2D Coordination Polymer for Enzyme-Free Electrochemical Glucose Sensing

*Xiaochen Fu,[a] Matthew Sale,[a] Bowen Ding,[a] William Lewis,[b] Debbie S. Silvester,[c] Chris D. Ling,[a] Deanna M. D'Alessandro[a]**

a School of Chemistry, The University of Sydney, Sydney, New South Wales 2006, Australia

b Sydney Analytical, Core Research Facilities, The University of Sydney, Sydney, New South Wales 2006, Australia

c School of Molecular and Life Sciences, Curtin University, GPOBox U1987, Perth 6845, Western Australia, Australia

*Corresponding Author: deanna.dalessandro@sydney.edu.au, phone +61 2 9351 3777, fax: +61 3 9351 3329

ABSTRACT: Regular detection of blood glucose levels is a critical indicator for effective diabetes management. Owing to the intrinsic highly sensitive nature of enzymes, the performance of enzymatic glucose sensors is typically impacted by unwanted dependencies on pH, temperature and humidity. Correspondingly, the development of robust enzyme-free glucose sensors is desired due to their potential to improve upon the operational flexibility of traditional systems. In this study, a new Coordination Polymer (CP) incorporating melamine (Mel), biphenyl-4,4′-dicarboxylate ($BPDC^{2-}$) co-ligands and Zn(II) metal nodes, $[Zn_2(BPDC)_1Mel_{0.5}\text{-}Mel_{0.5}]\cdot(DMF_{0.6})$ {denoted CP1}, was synthesised and characterized for non-enzymatic glucose sensing. Here, the 2D layers are connected by hydrogen bond (H-bond) interactions between the interstitial melamine molecules. In addition to conventional characterization methods, we also used density functional theory (DFT) calculations

and variable temperature Raman spectroscopy to computationally and experimentally explore the H-bond interactions in CP1. CP1 was deposited onto a glassy carbon (GC) electrode to facilitate its incorporation into an electrochemical sensing device. When used as an electrochemical glucose sensor, the CP1/GC electrode exhibited accurate clinical performance characteristics, with a wide linear sensing range extending from 5.6 μM to 5.56 mM (R^2 = 0.9852) with a high sensitivity of 517.36 μA mM^{-1} cm^{-2}. Low sample loadings are a further important advantage associated with this CP-based non-enzymatic glucose sensor.

KEYWORDS: coordination polymer, hydrogen bonded framework, density functional theory, electrochemistry, glucose sensor

1. INTRODUCTION

Monitoring blood sugar (glucose) concentrations is a requirement for the management of health issues such as diabetes.[1–3] Due to the intrinsic properties of enzymes, the performance of enzyme-based sensors depends on pH, temperature and humidity. [4–7] Therefore, non-enzymatic systems for glucose detection have been proposed, and are regarded as being more useful under a wider range of conditions and more readily adaptable to device fabrication.[8–13] In enzyme-free systems, redox couples such as Fe(II)/Fe(III) are used for catalyzing the transformation of glucose into gluconic acid.[14,15] Recently, many materials have been utilized as electrode surfaces for enzyme-free glucose sensing such as graphene, metal nanoparticles, coordination polymers (CPs) and their subclass, metal-organic frameworks (MOFs). [6,16–22] In the field of coordination chemistry, CPs have been developed for both enzyme-incorporated and enzyme-free sensing of glucose.[23,24] Apart from some open porous CPs, which can concentrate the analyte within their pores, [24–26] attractive features of CPs are their diverse chemistry and the tunability of their compositions, which enable the host-guest interactions to be modulated.[27]

An interesting strategy to develop enzyme-free glucose sensing involves the incorporation of melamine (Mel) into a CP to accumulate glucose via hydrogen-bonding interactions. Such interactions are well-known to occur between Mel and aminobenzoic acid, for example, during drug delivery. [28–31] Our present work reports a new 2D material incorporating Mel, which is itself known to be a component of CPs with multiple applications.[32,33] The CP CP1 is shown to engage in H-bonding interactions from both experimental and computational studies, as well as having good stability in aqueous systems between pH 7 and 8. Here we demonstrate that the material acts as an enzyme-free glucose sensor with a wide linear sensing range compared to previously published

materials employing precious metal Au, Pt nanoparticles (AuNPs and PtNPs) and other MOF related materials.[23,27,34–36] Raman and VT-Raman spectroscopy reveal that the highly concentrated hydrogen bond network pre-concentrates the glucose, thus efficaciously accumulating the analyte and allowing the detection of very low concentrations. We verified the sensing response under various pH conditions and compared the sensing properties to those of AuNPs, PtNPs and other materials (coated on GC electrodes) which are commonly used to catalyze electro-organic transformations.[37, 38, 36]

2. EXPERIMENTAL SECTION

2.1. Chemicals and Instrumentation. All starting materials were purchased from Sigma Aldrich and were used as received without further purification. The solvents were reagent grade. Powder X-ray diffraction (PXRD) patterns were recorded with a PANalytical X'Pert MPD (Cu Kα, λ=1.5418 Å) within the 2θ range 5-50° at room temperature. Thermogravimetric analysis (TGA) was carried out in a nitrogen stream using Hiden-Isochema IGA-002 gravimetric equipment with heating from room temperature up to 700 °C at a heating rate of 10 °C·min^{-1}. The electrochemical performance was measured with a Bioanalytical Systems (BASi) Potentiostat for cyclic voltammetry (CV) and differential pulse voltammetry (DPV). CV and DPV measurements were performed in 0.1 mM $K_3[Fe(CN)_6]/K_4[Fe(CN)_6]$ (1:1) solution containing 0.5 mM KCl at a scan rate of 100 mV/s (for CV) scanning the potential from 0 V to +0.5 V and back to 0 V. The parameters for DPV were: pulse width 50 ms, pulse period 200 ms, pulse amplitude 50 mV and step E 4 mV, scanning the potential from 0 V to 0.5 V. Additional details of electrodes are provided in Supporting Information. Raman spectra were collected using an inVia Renishaw Raman Spectrometer with 785 nm laser excitation (Argon ion). In situ variable temperature Raman (VT- Raman spectra) were collected using a Linkam stage, the temperature points from 25 to 50, 75, 100, 125, 150, 175, 200, 225, 250 ºC with a rate of

~7 ºC /min. All the samples were sealed in glass capillary (diameter 1 mm). Supporting spectra were recorded in S5 transmission mode with a frequency range of 600−3500 cm^{-1}.

2.2. Synthesis of CP1. $Zn(CH_3COO)_2 \cdot 2H_2O$(0.4 mM, 87.8 mg), 1,3,5-triazine-2,4,6-triamine (0.4 mM, 47.3 mg) and biphenyl-4,4′-dicarboxylic (0.6 mM, 145.3 mg) were added to a mixture of DMF and MeOH (in a ratio of 4:1=v/v, 10 ml) before the addition of 1% H_2O. The mixture was heated in the oven to 90 °C for 72 hours. The solution was cooled down to room temperature and the yellow hexagonal crystals were collected and sorted in DMF. Additional details of the synthesis and crystallographic data are provided in the Supporting Information. Crystal structure data can be obtained from the Cambridge Crystallographic Data Center (CCDC 2036487).

2.3. Electrochemical Sensing and Fabrication of modified GC Electrodes. The ground CP1 (10 mg) was dispersed in DMF (1 mL) to achieve a 10 mg/mL suspension and was sonicated for 5 minutes to form a homogeneous dispersion. The GC electrode (3 mm diameter) was polished with 0.3 um Al_2O_3 slurry, then sonicated in ethanol/water (1:1, v/v) solution 1 minute for 3 times. 10 µL of the suspension was drop-casted onto the surface of the GCE overnight and left to dry in air. Additional details of the electrode fabrication are provided in the Supporting Information.

2.3. Theoretical analysis of hydrogen bonding. H-bonding was studied using *ab-initio* density functional theory with the VASP program including the DFT-D3(BJ) empirical approximation to Van der Waals interactions, further details are provided in the Supporting Information. [39–44]

3. COMPUTATIONAL STUDIES

The refined crystal structure model indicates the presence of significant H-bonding in the framework. In order to gain further insight into the mechanism of H-bond interactions, we further studied H-

bonding at the atomic scale using *ab-initio* calculations. We applied *ab-initio* DFT-D3(BJ) calculations which include an empirical approximation to the Van der Waals force to simulate H-bonding in the intermolecular interactions. Further details are provided in the Supporting Information.[39–44]

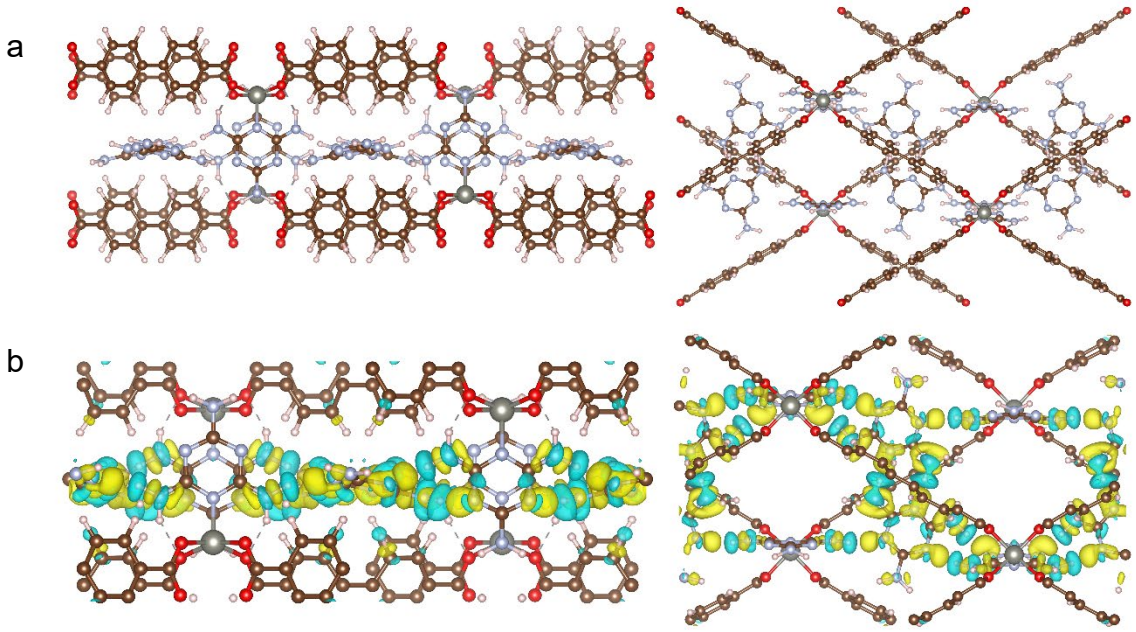

Figure 1. (a) Computational model of relaxed CP down the a-axis (left), down the c-axis (right). (b) Differential charge densities at an iso-level of 0.00094 electrons/Å^3 down the a-axis (left), down the c-axis (right). Yellow areas exhibit the charge accumulation. Blue areas exhibit the charge depletion upon connecting the layers together with interstitial melamine molecules as described in text. The visualized differential charge per layer of coordinated melamine and interstitial melamine shows that the framework layers were linked together by H-bonds.

The CP1 experimental structure was used as the starting point for calculations which contained dual layers of ZnBPDCMel 2D network and interstitial melamine molecules (Figure 1a), with a total of

456 atoms in 1 × 1 × 1 supercell (Figure S6). This structure also included the experimentally measured interstitial melamine which we investigated using *ab-initio* calculations to determine if it was H-bonded to the framework atoms. The geometry was relaxed according to the procedure in the Supporting Information and the details of bonding were analyzed using differential charge density and the electron localization function (ELF).

The geometry-optimized CP1 module showed an interplanar distance of 6.4 Å which is similar to the 6.7 Å distance from the experimental model, when measured between neighboring benzene molecules between layers. The geometry optimized structure was very similar to the experimental structure and confirmed the presence of N-H···N H-bonding between the interstitial melamine and the Zn(BPDC)Mel 2D framework. We identified three different types of N-H···N H-bonding as indicated in Figure 2c (with distances shown in Table S1, which also show the comparison to the experimental values). This shows that each interstitial melamine molecule is H-bonded to its neighbor with two H-bonds (H52···N27, H51···N28) to form a dimer and is also H-bonded to the framework via the coordinated melamine with single H-bonds on opposite sides (N20···H68 and N19···H67, N71···H3 and N72···H4, N79···H23 and N80···H24). The interstitial melamine molecules are not connected to the Zn(BPDC)Mel layers though coordination bonds. These length values show good agreement between the calculated and experimental N-H···N hydrogen bonding distances and are in good agreement with the range of conventional H-bond interactions.

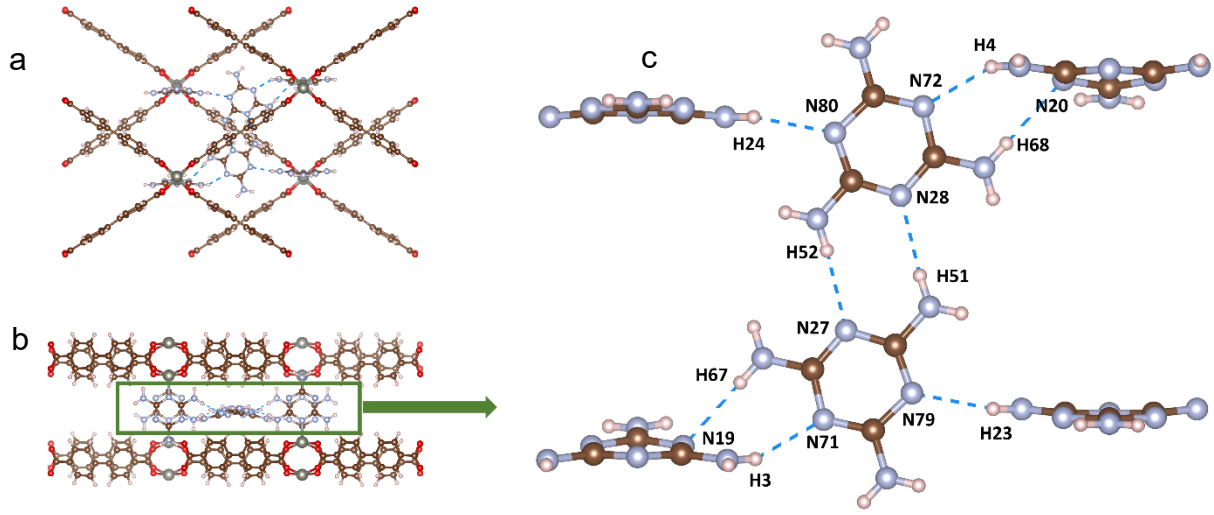

Figure 2. The geometry optimized model of CP1 CP using VASP5.4.4 showing an environment of the N-H···N H-bonds which attach the free melamine to the CP framework as labeled in the diagram. (a) The orientation of the melamine network to the Zn(BPDC)Mel 2D framework down the c-axis and, (b), down the a-axis. (c) A section of the melamine H-bonding network looking down the c-axis.

Table S1 shows 4 types of simulated H-bond lengths which are 1.8 Å (H52···N27, H51···N28), 1.9 Å (H68··· N20, H67··· N19), 2.2 Å (H3··· N71, H4··· N72) and 2.06 Å (H23··· N79, H24··· N80) (Figure 2c). The differential charge density shows how electrons are increased when interacting and forming H-bonds and was calculated as follows (see Figure 1b). The charge density of each of the four individual interstitial melamine and the Zn(BPDC)Mel 2D network were separately calculated and summed to form a charge density without interlayer bonding. This was then subtracted from the original charge density to produce the differential charge density. The latter shows the charge density rearrangement connecting the 2D sheet layers and interstitial melamine molecules together, and helps to identify bond formation and/or interactions.[45,46] Figure 1b shows the accumulation of electron density around the nitrogen atoms and depletion around hydrogen atoms, providing strong evidence

of the H-bond interaction. The change in charge density is mostly concentrated on the N atoms of both coordinated and interstitial melamine without the NH_2 functional groups. The differential charge densities along with the bond distances show that the 2D sheet layers of the CP are more strongly held together by the N-H···N hydrogen bonds.

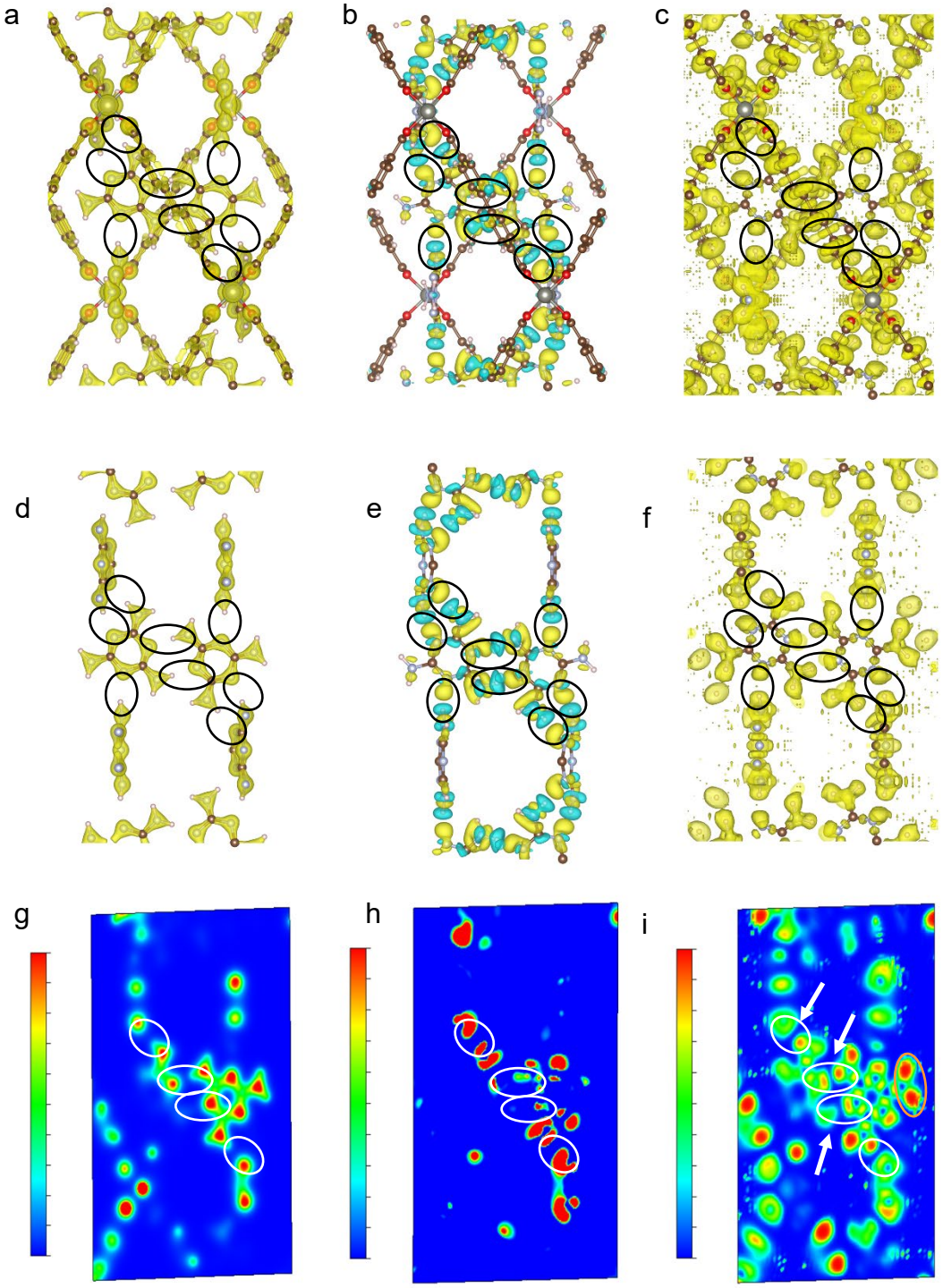

Figure 3. Comparison between 3D model and interstitial melamine cut plane figure for charge density (a, d and g), differential charge density (b, e and h) and Electron Localization Function (c, f and i). A section of the melamine H-bonding looking down the c-axis (d, e and f). Cut plane through the one of the two interstitial melamine molecules (right) in the crystal (g, h and i). The blue/red represents low/high values of 2D slides of charge density, differential charge density and ELF respectively, which are restricted by construction in the region of [0, 1]. Black circles (a, b, c, d, e, and f) indicate all the hydrogen bonding and white circles (g, h and i as white arrow indicates) indicate hydrogen bonding on the cut plane of the right interstitial melamine molecule.

Furthermore, the ELF is widely applied to analyze intermolecular interactions and bonds.[47] This method provides an accurate theoretical method for analyzing these interactions as it provides visualization of the Pauli exclusion principle and kinetic energy for electron localization.[48] We therefore focused on investigating the N-H···N bond using the ELF; this provides additional information on the charge density, which reveals electron localization, and the differential charge density, which indicates the extent of electron transfer.

As can be seen in the cut plane of the CP1 in Figure 3i, the bonds between the two interstitial melamine molecules and between the coordinated and interstitial melamine molecules are bound through H-bonds. All of these bonds exhibit the features of both electron localization and partial electron delocalization. Specifically, at the bonds between melamine dimers (1.8 Å, H52···N27, H51···N28, indicated at white circles in Figure 3i), the blue gap indicates electron localization (i.e., no direct covalent bond is observed) between the nitrogen atom in the triazine and the hydrogen in the NH_2 group. The ionic nature of the N-H···N hydrogen bonds is also clearly seen as the electrons

are highly localized at the hydrogen nucleus. However, some additional electron delocalization of these hydrogen and nitrogen bonds can also be clearly seen by comparing them with the fully unbonded NH_2 group on the right (Figure 3i, orange circle): the degree of localization decreases significantly when hydrogen bonded to its neighbor. Also, the nitrogen-hydrogen bonds show a trend of electron accumulation around the nitrogen atom. Therefore, it was observed that the electrons of the hydrogens on the melamine molecules were attracted to the nitrogen atoms in the triazine ring of the neighboring melamine via H-bonding. Here, the result of ELF further supports the presence of a bridging N-H···N hydrogen bond between neighboring melamine molecules.

4. RESULTS AND DISCUSSION

4.1. Structural description. Hexagonal prism-shaped crystals of CP1 were obtained as detailed in SI section 2. Single-crystal X-ray analysis revealed that this CP1 crystallizes in the orthorhombic space group *Abm*2. The material displays a 2D sheet structure with Mel hydrogen-bonded within the framework unit. The asymmetric unit consists two Zn(II) ions, two $BPDC^{2-}$ ligands, two Mel ligands and one interstitial Mel molecule. Both Zn(II) ions are five-coordinate and are bound by four carboxylate oxygen atoms from BPDC ligands and one nitrogen atom from melamine molecule. The Zn(1)–O bond lengths are in the range of 2.018(5) to 2.040(4) Å and the Zn(2)–O bond lengths are in the range 2.032(4) to 2.060(4) Å. The Zn(1)-N bond length is 2.027 Å and the Zn(2)-N bond length is 2.026 Å. The Zn(II) centers exhibit a paddle wheel-shaped dinuclear $\{Zn_2(COO)_4\}$ sub-unit with four bis-monodentate carboxylate groups of $BPDC^{2-}$ ligands, capped by two coordinated Mel molecules. These sub-units are bridged together by $BPDC^{2-}$ forming a 2D sheet in the *bc*-plane (Figure 4c). The 2D sheets are connected via the coordinated Mel through H-bonding to uncoordinated Mel molecules, which stabilize the multi-layer structure of this CP.

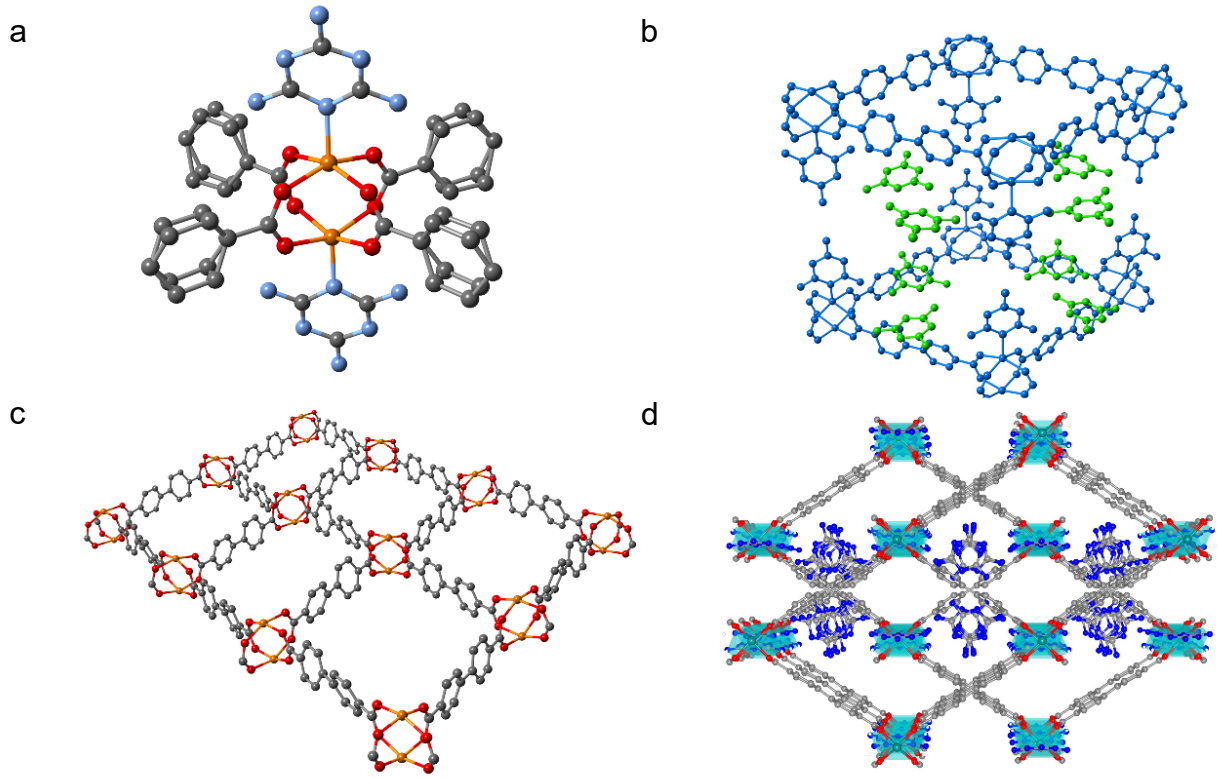

Figure 4. (a) View of Zn(II) coordination environments in CP1, showing the dinuclear paddle wheel unit. (b) View of additional interstitial Melamine molecules in the pores of CP1 (green) which form strong H-bonds with Zn(BPDC)Mel 2D framework (shown in blue) and assist in stabilizing the overall structure. (c) View of the 2D sheets of $BPDC^{2-}$ co-ligands and Zn(II) nodes.(d) View of the rendered structure shows the position of additional interstitial Mel between Zn(BPDC)Mel 2D sheets down the c-axis. For (a), (c) and (d), grey = carbon, red = oxygen, yellow = zinc, blue = nitrogen. For all images hydrogen atoms were omitted for clarity.

Considering the intended application of this material as a glucose sensor, the stability of CP1 in water and weak base and acid was studied. Figure 5 shows the normalised PXRD patterns of unsoaked CP1 (Figure 5, grey line i), the material immersed in water for 7 days (Figure 5, green line ii) and 14 days (Figure 5, yellow line iii), the material immersed in a weak base (pH 8, Figure 5, deep blue line iv)

and weak acid (pH 6, Figure 5, red line v) for 2 hours. The patterns show the same diffraction peaks, supporting the stability of the framework in water and weak base where the result shows its capacity to be applied in aqueous phase electrochemical sensing under weak base condition.

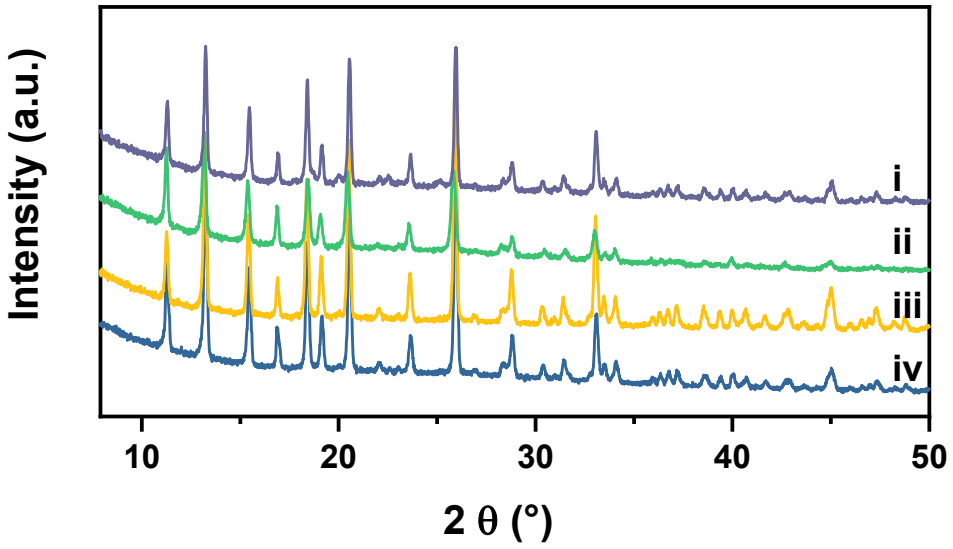

Figure 5. Comparison of PXRD patterns for (i) CP1, (ii) immersed in water for 7 days, (iii) and 14 days; (iv) immersed in weakly base solution for 2 hours (pH 8).

4.2. Raman Spectroscopic Studies. Despite a number of published detection methods including Raman spectroscopy (room temperature) for interlayer H-bond characterization in CPs,[12,18−20] there are still some barriers to direct H-bond characterization in CPs. Due to the presence of H-bonding interactions, we investigated the Raman shift of peaks associated with functional groups that were directly involved in these interactions. According to published studies on amide contained materials studies,[38−40] owing to the N−H bond order increasing as the result of hydrogen bonding disruption at high temperatures, the frequency of N−H shifts to lower wavenumbers (i.e., a red shift). Thus, the variable temperature Raman analysis (VT-Raman, Figure 6a) was applied to directly analyze these H-bonding interactions in the crystal. In the present VT-Raman analysis, data were collected

following the temperature range from 25 °C (room temperature) to 250 °C. As the sample was heated, the vibrational frequency that corresponds to the amide N−H shifted to lower frequency (Figure 6a) with no effect on the other vibrational peaks in the spectrum. At 25 °C, the amide N−H vibrational peak（δNH_2）of CP1 appears at 1609 cm^{-1} (position 1, Figure 6a). When the temperature reaches 250 °C, the peak has shifted to 1603 cm^{-1} (position 2) with an overall shift of 6 cm^{-1} (Figure 6a), and has also broadened with the FWHM changing from 1609 cm^{-1} at 25 °C to 1603 cm^{-1} at 250 °C. This temperature dependent shift could due to the formation of free N−H sites leading to an increase in the N−H bond order and the disruption of H−bonding.

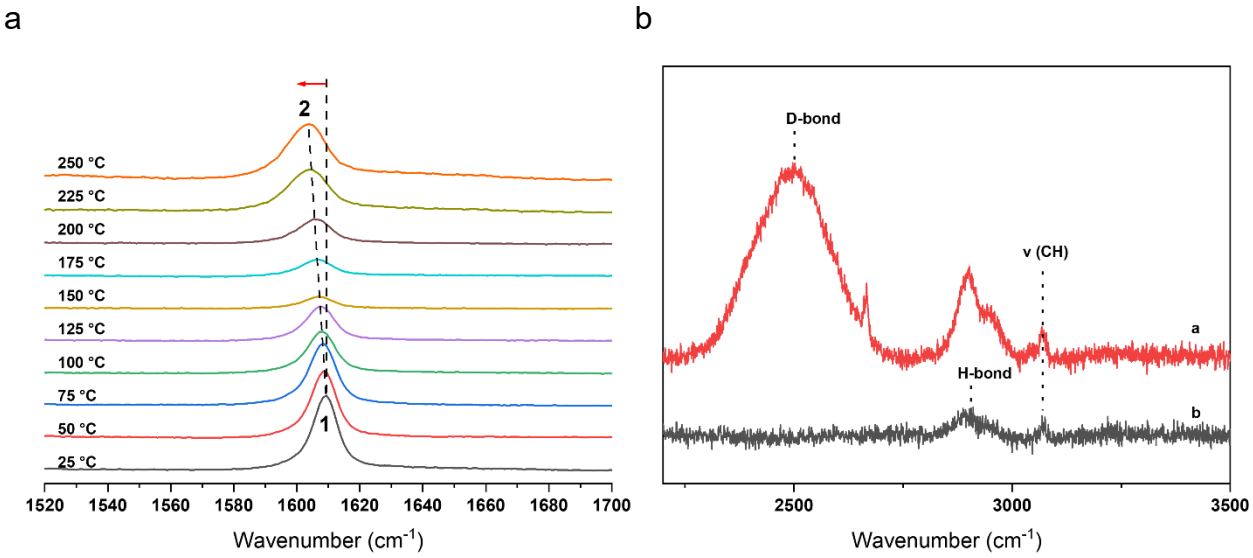

Figure 6. **(a)** Variable temperature Raman spectra of a single crystal of CP1, showing the expanded amide N−H stretching region. The red arrow indicates the shift in the peak at 1609 to 1603 cm^{-1}. (b) Raman spectra of CP1 immersed in D_2O (red) and H_2O (black) as solvents for glucose solution in the high frequency region. The weak broad band due to hydrogen bonding vibrations from water was also shifted to lower frequencies.

In a further study, we analysed original and deuterated Raman spectra of CP1 crystals immersed in glucose solution with either H_2O or D_2O as solvent. Spectra in the higher frequency region are presented in Figure 6b. It can be seen that all bands are shifted for the crystal in D_2O-glucose solution, except the stretching vibrations from CH bonds where the hydrogen atom was not replaced by deuterium (Figure 6b). The assignment of the weak but broad band to vibrations of water in the hydrogen bond was confirmed by its shift in the deuterated composite.[49–51] These modes depend on the moment of inertia which is approximately two times larger for D_2O solution than for H_2O, such that the frequency of the band of D_2O is reduced by a ratio of approximately 1.414. The ratio of frequency for two vibrations in D_2O and H_2O solution is about 1.14. These observations provide further convincing evidence that the material H-bonds with glucose in the aqueous phase, and that water molecules are a part of the crystal matrix in the solution.

4.3. Glucose sensing. Cyclic voltammetry (CV) and differential pulse voltammetry (DPV) were used to monitor the formation of the CP1 layer on the glassy carbon (GC) electrode and gain insight into the corresponding electron transfer reaction (Figure 7). Note here that DPV was employed owing to its high sensitivity as an electrochemical measurement technique.[52] $K_3[Fe(CN)_6]/K_4[Fe(CN)_6]$ (1:1, 0.1 mM) was also introduced in KCl solution as an electron mediator in the buffer system as described in section 2.1, with pH 7.5 determined as the most appropriate pH (Figure 8b). Figure 7a shows the comparison of a bare GC electrode (black) and the modified electrodes. The CV response of CP1/GC was significantly lower than that of the bare electrode, indicating that the CP1 had formed a film on the electrode surface. DPVs demonstrating glucose detection at various concentrations are shown for the modified electrode in Figure 7b.

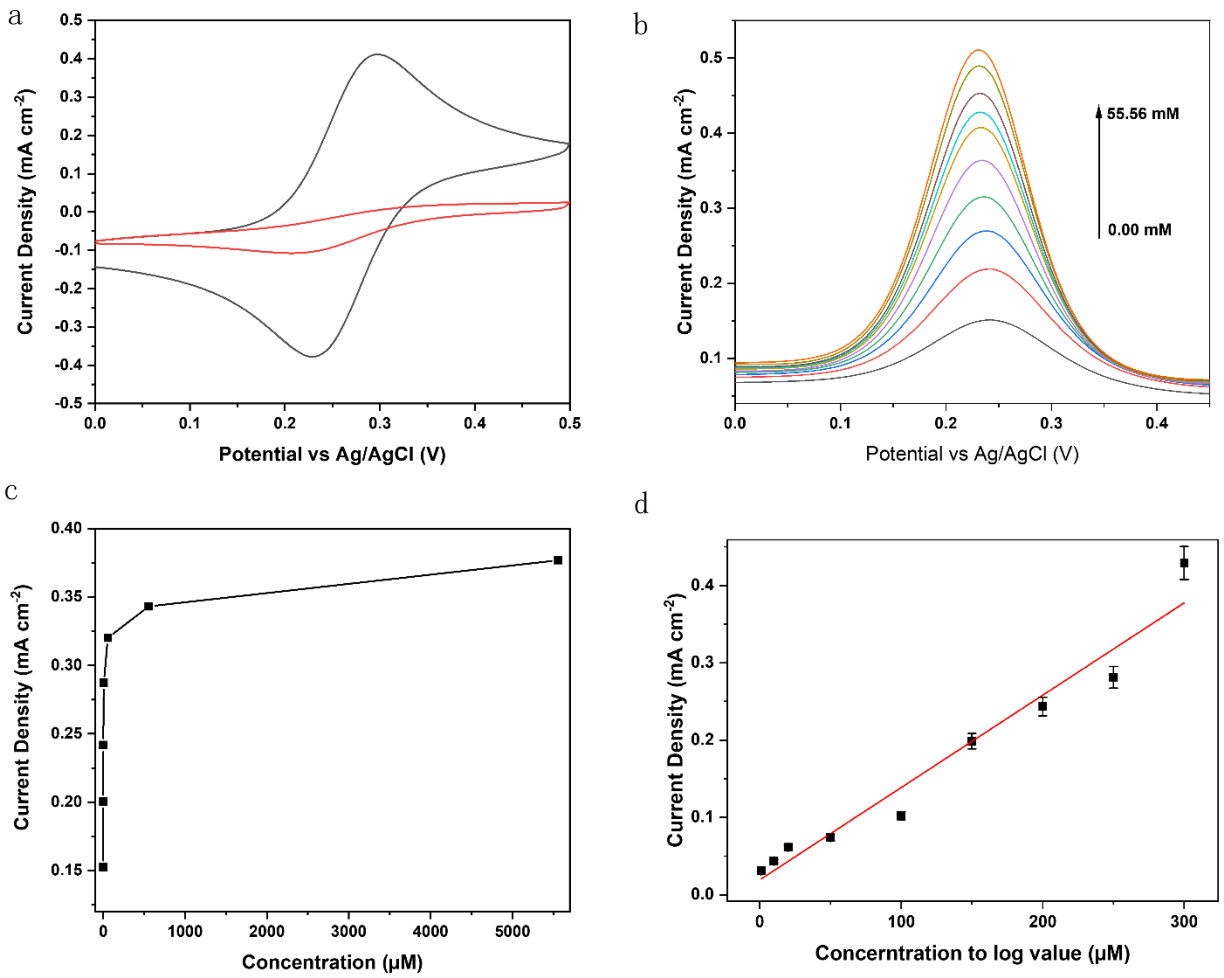

Figure 7. (a) CV characterization of the modified electrode in $K_3[Fe(CN)_6]/K_4[Fe(CN)_6]$ solution containing 0.5 mM KCl at pH 7: bare electrode (i, red), CP1/GC (ii, black), scan rate 100mV/s; (b) DPV performance of CP1 modified electrode from 0 mM to 55.56 mM in $K_3[Fe(CN)_6]/K_4[Fe(CN)_6]$ solution containing 0.5 mM KCl at pH 7.5 for glucose detection; (c) Plots of the current density versus the concentration of glucose ($c_{glucose}$); (d) the curve of the linear current density on the log value of $c_{glucose}$, $R^2 = 0.9852$) with the linear range from 0 to 5.56 mM; error bars denote standard deviation for 3 measurements.

CV was applied for monitoring the fabrication of the adsorption layer on GC electrode corresponding the electron transfer. Figure 7a shows the different response between the bare electrode and CP1/GC in $K_3[Fe(CN)_6]/K_4[Fe(CN)_6]$ solution containing 0.5 mM KCl. The bare electrode shows a higher CV response than CP1/GC, indicating, as noted in previous works, that CP1 formed a thin layer on the electrode surface.[53] Figure 7b shows a series of DPVs for glucose over the concertation range from 0.00 mM to 55.56 mM containing the $[Fe(CN)_6]^{3/4-}$ couple at 0.1 mM KCl solution at pH 7.5.[11] The electrochemical peak current for CP1/GC displayed a linear relationship with $log_{10}\, c_{glucose}$ (Figure 7c, d) from 5.6 µM to 5.56 mM with a high sensitivity of 517.36 µA mM^{-1} cm^{-2} (R^2 = 0.9852), and a detection limit of 0.56 µM. Table 1 illustrates the different performance of MOF based material and metal nano particles composite for electrochemical glucose sensing. [32,50–60] As can be seen, apart from the graphene/PtNP based sensor with extremely high conductivity[54], Table 1 clearly shows that the CP1 based electrochemical sensor demonstrates a wider linear range with a good limit of detection (LOD) compared with other enzymic-free glucose sensors based on pristine MOFs, MOF/carbon material composites and MOF/metal nano particles/carbon material composites. Our CP1 exhibits a better linear range without the need for addition of highly conductive materials.

Table 1. Comparison of different materials (MOF, MOF composite and other materials) used as electrodes, and the analytical performance obtained for non-enzymatic glucose sensing.

Modified material	Linear range (μM)	LOD (μM)	Ref.
GOx/PtNP/PANI/Pt[a]	10–8000	0.7	[54]
GOx/MOFs/PtNPS[b]	5–1400	5	[55]
Cu-in-ZIF-8/SPCE[c]	0–700	2.76	[36]
CoII-MOF/Acb-0.2%/GCE[d]	5–1000	1.7	[56]
Ni-MOF/Ni/NiO/C	4–566	0.8	[57]
Ni-MIL-77	1–500	0.25	[58]
Eu-pydc[e]	10-1000	6.9	[59]
MOF-71	50-1000	15.61	[60]
Ni-BDC MOF	10-800	6.68	[61]
ZIF-67	5-3300, 3300-42100	0.96	[62]
ZIF-74	1-1000	0.41	[63]
$Mn_2\{Ni(C_2S_2(C_6H_4COO)_2)_2\}(H_2O)_2$	2-2000	0.1	[64]
CP1[f]/GC	5-5560	0.56	This work

*a Pt nanoparticles (PtNPs), polyaniline (PANI);b Pt nanoparticles (PtNPS);c screen-printed carbon electrodes (SPCE);d CoII-MOF/acetylene black (CoII-MOF/Acb);e pydcd-2,5-pyridinedicarboxylic acid; f Zn(BPDC)Mel: melamine (Mel) ligands, biphenyl-4,4′-dicarboxylic acid ($BPDC^{2-}$)

A further challenge for glucose sensing applications is the potential of interference from other electrochemically-active analytes within a complex mixture such as human blood. Thus, the DPV

responses of the CP1/GC electrodes were tested with common substances in human blood which are ascorbic acid (AA), uric acid (UA) and dopamine (DA). The concentration of AA an UA in healthy humans is between 0.125 and 0.33 mM,[65,66] the concentration of DA in healthy blood is between 0.12–0.45 mM.[67] On the basis of published work, in human blood, the glucose level is 10 times higher than the concentration of interference substances.[18] The anti-interference performance was investigated using 0.56 mM glucose with 0.1 mM AA, 0.1 mM UA and 0.1 mM DA, in order to examine the selectivity of the CP1/GC electrode, which were added into the detection cell in order (Figure 8a). It was found that the AA, UA and DA substrates produced minimal responses, indicating that the CP1/GC electrode maintains good selectivity for glucose. This result is attributed to the interaction between Mel and glucose[68–70] through H-bonding by assisting the $K_3[Fe(CN)_6]/K_4[Fe(CN)_6]$ charge transfer and catalysis. The results also indicate that this CP may facilitate pre-concentration of glucose from the solution to the electrode surface, thus promoting its performance for glucose sensing.

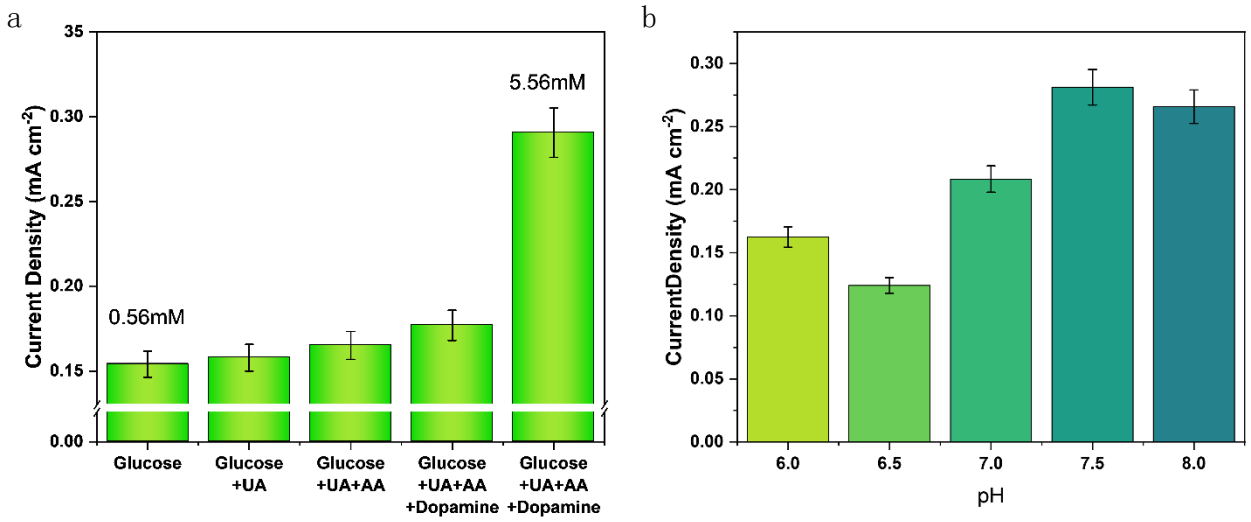

Figure 8. (a) The DPV current density difference (baseline subtracted) of the CP1/GC electrode towards the addition of glucose from 0.56 mM up to 5.56 mM glucose with 0.1 mM interference

substances, ascorbic acid (AA), uric acid (UA) and dopamine (DA). (b) Current density (baseline subtracted) to a glucose concentration of 0.056 μM under different pH conditions. Here, it was established that pH 7.5 was optimal for the highest current responses.

To further evaluate the performance of CP1/GC, we analyzed the reproducibility of this sensor. The current density of 5 mM glucose with the same CP1/GC was measured for 3 times, and the relative standard deviation (RSD) was 6.8%; the current density RSD of 3 independent CP1/GC electrodes to 5 mM glucose was 5.1% (Figure S11a), which indicates its reproductivity. In addition, with measurements taken every 15 days, the sensor retains 90.7% of its original value over a month (Figure S11b), which indicates its stability.

4. CONCLUSIONS

A new triazine-based CP (CP1) constructed from a network of extended 2D sheets, held together by H-bonding through free melamine between each layer, was developed in this study for its application in non-enzymatic glucose sensing. Due to the specific structure of CP1, the 2D layers were connected through both coordinated melamine and interstitial melamine molecules via H-bonding, which promotes interlayer interactions in the framework. We computationally and experimentally proved the existence of hydrogen bonding interactions in the crystal with VASP calculations and VT-Raman experiments. Results from Raman spectroscopy demonstrated that hydrogen-bonding interactions, well known to occur between Mel and glucose,[68–70] may aid in pre-concentrating the glucose and promoting interactions between the redox mediator, $K_3[Fe(CN)_6]$/ $K_4[Fe(CN)_6]$, and glucose (Figure S9). The stability of CP1 in weak base and weak acid provides a basis for its application in aqueous sensing. An electrochemical non-enzymatic glucose sensing system was successfully fabricated with CP1 deposited onto GC, which exhibited excellent sensing characteristics, with a linear detection

range from 5.6 μM to 5.56 mM of glucose and a very low loading of CP1 of 80 μg (8 μL, 10 mg/ml). The low cost of the ligand and its low toxicity make CP1 a promising platform for further diversification into sensing and drug delivery systems.

ASSOCIATED CONTENT

Supporting Information

The Supporting Information is available free of charge on the ACS Publications website at DOI:

Experimental details of the synthesis of compounds, method of modifying electrode, crystal information, calculation, fabrication of the electrode, sensing, and characterization information (PDF)

AUTHOR INFORMATION

Corresponding Author: Deanna M. D'Alessandro

*E-mail: deanna.dalessandro@sydney.edu.au

Phone +61 2 9351 3777, fax: +61 3 9351 3329

ORCID

Xiaochen Fu: 0000-0003-0002-1795

William Lewis: 0000-0001-7103-6981

Chris D. Ling: 0000-0003-2205-3106

Debbie S Silvester: 0000-0002-7678-7482

*Deanna M. D'Alessandro: 0000-0002-1497-2543

Notes

The authors declare no competing financial interest.

ACKNOWLEDGEMENTS

The authors gratefully acknowledge the support of the Australian Research Council.

REFERENCES

(1) Bakh, N. A.; Cortinas, A. B.; Weiss, M. A.; Langer, R. S.; Anderson, D. G.; Gu, Z.; Dutta, S.; Strano, M. S. Glucose-Responsive Insulin by Molecular and Physical Design. *Nat. Chem.* **2017**, *9* (10), 937–943. https://doi.org/10.1038/nchem.2857.

(2) Pfützner, A.; Musholt, P. B.; Schipper, C.; Demircik, F.; Hengesbach, C.; Flacke, F.; Sieber, J.; Forst, T. Blood Glucose Meters Employing Dynamic Electrochemistry Are Stable against Hematocrit Interference in a Laboratory Setting. *J. Diabetes Sci. Technol.* **2013**, *7* (6), 1530–1537. https://doi.org/10.1177/193229681300700613.

(3) Bruen, D.; Delaney, C.; Florea, L.; Diamond, D. Glucose Sensing for Diabetes Monitoring: Recent Developments. *Sensors (Switzerland)* **2017**, *17* (8), 1–21. https://doi.org/10.3390/s17081866.

(4) Deng, Q.; Dong, S. Construction of a Tyrosinase-Based Biosensor in Pure Organic Phase. *Anal. Chem.* **1995**, *67* (8), 1357–1360. https://doi.org/10.1021/ac00104a009.

(5) Xu, X.; Wu, P.; Xu, W.; Shao, Q.; An, L.; Zhang, H.; Cai, C.; Zhao, B. Effects of Guanidinium Ions on the Conformational Structure of Glucose Oxidase Studied by Electrochemistry, Spectroscopy, and Theoretical Calculations: Towards Developing a Chemical-Induced Protein Conformation Assay. *Phys. Chem. Chem. Phys.* **2012**, *14* (16), 5824–5836. https://doi.org/10.1039/c2cp24121h.

(6) Pinyou, P.; Blay, V.; Muresan, L. M.; Noguer, T. Enzyme-Modified Electrodes for Biosensors and Biofuel Cells. *Mater. Horizons* **2019**. https://doi.org/10.1039/c9mh00013e.

(7) Wang, M.; Zheng, J.; Wang, L.; Dong, S. Direct Electrochemistry of Glucose Oxidase

Immobilized on Titanium Carbide-Au Nanoparticles-Fullerene C 60 Composite Film and Its Biosensing for Glucose. *J. Chinese Chem. Soc.* **2012**, *59* (8), 1006–1014. https://doi.org/10.1002/jccs.201100729.

(8) Li, Y.; Xie, M.; Zhang, X.; Liu, Q.; Lin, D.; Xu, C.; Xie, F.; Sun, X. Co-MOF Nanosheet Array: A High-Performance Electrochemical Sensor for Non-Enzymatic Glucose Detection. *Sensors Actuators, B Chem.* **2019**, *278* (August 2018), 126–132. https://doi.org/10.1016/j.snb.2018.09.076.

(9) Wu, L.; Lu, Z.; Ye, J. Enzyme-Free Glucose Sensor Based on Layer-by-Layer Electrodeposition of Multilayer Films of Multi-Walled Carbon Nanotubes and Cu-Based Metal Framework Modified Glassy Carbon Electrode. *Biosens. Bioelectron.* **2019**, *135* (March), 45–49. https://doi.org/10.1016/j.bios.2019.03.064.

(10) Wang, Q.; Zhang, X.; Huang, L.; Zhang, Z.; Dong, S. GOx@ZIF-8(NiPd) Nanoflower: An Artificial Enzyme System for Tandem Catalysis. *Angew. Chemie - Int. Ed.* **2017**, *56* (50), 16082–16085. https://doi.org/10.1002/anie.201710418.

(11) He, J.; Yang, H.; Zhang, Y.; Yu, J.; Miao, L.; Song, Y.; Wang, L. Smart Nanocomposites of Cu-Hemin Metal-Organic Frameworks for Electrochemical Glucose Biosensing. *Sci. Rep.* **2016**, *6* (August), 1–9. https://doi.org/10.1038/srep36637.

(12) Ci, S.; Huang, T.; Wen, Z.; Cui, S.; Mao, S.; Steeber, D. A.; Chen, J. Nickel Oxide Hollow Microsphere for Non-Enzyme Glucose Detection. *Biosens. Bioelectron.* **2014**, *54*, 251–257. https://doi.org/10.1016/j.bios.2013.11.006.

(13) Jeong, R. A.; Hwang, J. Y.; Joo, S.; Chung, T. D.; Park, S.; Kang, S. K.; Lee, W. Y.; Kim, H. C. In Vivo Calibration of the Subcutaneous Amperometric Glucose Sensors Using a Non-Enzyme Electrode. *Biosens. Bioelectron.* **2003**, *19* (4), 313–319.

https://doi.org/10.1016/S0956-5663(03)00219-7.

(14) Wang, W.; Kong, L.; Zhu, J.; Tan, L. One-Pot Preparation of Conductive Composite Containing Boronic Acid Derivative for Non-Enzymatic Glucose Detection. *J. Colloid Interface Sci.* **2017**, *498*, 1–8. https://doi.org/10.1016/j.jcis.2017.03.040.

(15) Toghill, K. E.; Compton, R. G. Electrochemical Non-Enzymatic Glucose Sensors: A Perspective and an Evaluation. *Int. J. Electrochem. Sci.* **2010**, *5* (9), 1246–1301.

(16) Chen, W.; Vázquez González, M.; Zoabi, A.; Abu Reziq, R.; Willner, I. Biocatalytic Cascades Driven by Enzymes Encapsulated in Metal–Organic Framework Nanoparticles. *Nat. Catal.* **2018**, *1* (9), 689–695. https://doi.org/10.1038/s41929-018-0117-2.

(17) Deng, C.; Chen, J.; Chen, X.; Xiao, C.; Nie, L.; Yao, S. Direct Electrochemistry of Glucose Oxidase and Biosensing for Glucose Based on Boron-Doped Carbon Nanotubes Modified Electrode. *Biosens. Bioelectron.* **2008**, *23* (8), 1272–1277. https://doi.org/10.1016/j.bios.2007.11.009.

(18) Song, J.; Xu, L.; Zhou, C.; Xing, R.; Dai, Q.; Liu, D.; Song, H. Synthesis of Graphene Oxide Based Cuo Nanoparticles Composite Electrode for Highly Enhanced Nonenzymatic Glucose Detection. *ACS Appl. Mater. Interfaces* **2013**, *5* (24), 12928–12934. https://doi.org/10.1021/am403508f.

(19) Kumar, R. NiCo(2)O(4) Nano-/Microstructures as High-Performance Biosensors: A Review. *Nano-micro Lett.* **2020**, *12* (1), 122. https://doi.org/10.1007/s40820-020-00462-w.

(20) Safadi, B. N.; Gonçalves, J. M.; Castaldelli, E.; Matias, T. A.; Rossini, P. O.; Nakamura, M.; Angnes, L.; Araki, K. Lamellar FeOcPc-Ni/GO Composite-Based Enzymeless Glucose Sensor. *ChemElectroChem* **2020**, *7* (12), 2553–2563. https://doi.org/10.1002/celc.202000138.

(21) Gorle, D. B.; Ponnada, S.; Kiai, M. S.; Nair, K. K.; Nowduri, A.; Swart, H. C.; Ang, E. H.; Nanda, K. K. Review on Recent Progress in Metal–Organic Framework-Based Materials for Fabricating Electrochemical Glucose Sensors. *J. Mater. Chem. B* **2021**, *9* (38), 7927–7954. https://doi.org/10.1039/d1tb01403j.

(22) Teymourian, H.; Barfidokht, A.; Wang, J. Electrochemical Glucose Sensors in Diabetes Management: An Updated Review (2010–2020). *Chem. Soc. Rev.* **2020**, *49* (21), 7671–7709. https://doi.org/10.1039/d0cs00304b.

(23) Zhang, Y.; Xu, J.; Xia, J.; Zhang, F.; Wang, Z. MOF-Derived Porous Ni 2 P/Graphene Composites with Enhanced Electrochemical Properties for Sensitive Nonenzymatic Glucose Sensing. *ACS Appl. Mater. Interfaces* **2018**, *10* (45), 39151–39160. https://doi.org/10.1021/acsami.8b11867.

(24) Guo, Q.; Ren, L.; Kumar, P.; Cybulskis, V. J.; Mkhoyan, K. A.; Davis, M. E.; Tsapatsis, M. A Chromium Hydroxide/MIL-101(Cr) MOF Composite Catalyst and Its Use for the Selective Isomerization of Glucose to Fructose. *Angew. Chemie - Int. Ed.* **2018**, *57* (18), 4926–4930. https://doi.org/10.1002/anie.201712818.

(25) Yi, X.; Dong, W.; Zhang, X.; Xie, J.; Huang, Y. MIL-53(Fe) MOF-Mediated Catalytic Chemiluminescence for Sensitive Detection of Glucose. *Anal. Bioanal. Chem.* **2016**, *408* (30), 8805–8812. https://doi.org/10.1007/s00216-016-9681-y.

(26) Duan, Y.; Ye, F.; Huang, Y.; Qin, Y.; He, C.; Zhao, S. One-Pot Synthesis of a Metal-Organic Framework-Based Drug Carrier for Intelligent Glucose-Responsive Insulin Delivery. *Chem. Commun.* **2018**, *54* (42), 5377–5380. https://doi.org/10.1039/c8cc02708k.

(27) Kang, Z.; Jiao, K.; Peng, R.; Hu, Z.; Jiao, S. Al-Based Porous Coordination Polymer Derived Nanoporous Carbon for Immobilization of Glucose Oxidase and Its Application in

Glucose/O2 Biofuel Cell and Biosensor. *RSC Adv.* **2017**, *7* (20), 11872–11879. https://doi.org/10.1039/c7ra00852j.

(28) Tantishaiyakul, V.; Dokmaisrijan, S.; Sangfai, T.; Hirun, N.; Li, L.; Juntarapet, S.; Suknuntha, K. Investigation of the Efficiency of Gelation of Melamine with the Positional Isomers of Aminobenzoic Acid. *Colloids Surfaces A Physicochem. Eng. Asp.* **2014**, *446*, 118–126. https://doi.org/10.1016/j.colsurfa.2014.01.051.

(29) Wang, J.; Ma, D.; Liao, W.; Li, S.; Huang, M.; Liu, H.; Wang, Y.; Xie, R.; Xu, J. A Hydrostable Anionic Zinc-Organic Framework Carrier with a Bcu Topology for Drug Delivery. *CrystEngComm* **2017**, *19* (35), 5244–5250. https://doi.org/10.1039/c7ce01238a.

(30) Du, X.; Fan, R.; Qiang, L.; Xing, K.; Ye, H.; Ran, X.; Song, Y.; Wang, P.; Yang, Y. Controlled Zn2+-Triggered Drug Release by Preferred Coordination of Open Active Sites within Functionalization Indium Metal Organic Frameworks. *ACS Appl. Mater. Interfaces* **2017**, *9* (34), 28939–28948. https://doi.org/10.1021/acsami.7b09227.

(31) Li, F.; Li, B.; Wang, C.; Zeng, Y.; Liu, J.; Gu, C. Y.; Lu, P.; Mei, L. Encapsulation of Pharmaceutical Ingredient Linker in Metal-Organic Framework: Combined Experimental and Theoretical Insight into the Drug Delivery. *RSC Adv.* **2016**, *6* (53), 47959–47965. https://doi.org/10.1039/c6ra06178h.

(32) Zhang, L.; Yang, W.; Wu, X. Y.; Zhang, G. H.; Lu, C. Z.; Chen, W. Z. A Microporous Cobalt-Organic Framework Constructed from Mixed Tripodal Ligands for High CO2 Adsorption Capacity. *Inorg. Chem. Commun.* **2016**, *68*, 60–62. https://doi.org/10.1016/j.inoche.2016.04.004.

(33) Zhang, J.; Li, Z.-J.; Wen, Y.-H.; Kang, Y.; Cheng, J.-K.; Yao, Y.-G. Syntheses and Structures of Two Novel Ag(I) Complexes: [M3-2-(4-Pyridyl)Ethanesulfonato-N,O,O′]-

Aqua-Silver(I) and Melamine-[2-(4-Pyridyl)Ethanesulfonato-N]-Silver(I). *J. Mol. Struct.* **2004**, *697* (1–3), 185–189. https://doi.org/10.1016/j.molstruc.2004.04.009.

(34) Mao, X.; Lu, Y.; Zhang, X.; Huang, Y. β-Cyclodextrin Functionalization of Metal-Organic Framework MOF-235 with Excellent Chemiluminescence Activity for Sensitive Glucose Biosensing. *Talanta* **2018**, *188* (May), 161–167. https://doi.org/10.1016/j.talanta.2018.05.077.

(35) Paul, A.; Srivastava, D. N. Amperometric Glucose Sensing at Nanomolar Level Using MOF-Encapsulated TiO 2 Platform. *ACS Omega* **2018**, *3* (11), 14634–14640. https://doi.org/10.1021/acsomega.8b01968.

(36) Shi, L.; Zhu, X.; Liu, T.; Zhao, H.; Lan, M. Encapsulating Cu Nanoparticles into Metal-Organic Frameworks for Nonenzymatic Glucose Sensing. *Sensors Actuators, B Chem.* **2016**, *227*, 583–590. https://doi.org/10.1016/j.snb.2015.12.092.

(37) Wu, L.; Lu, X.; Fu, X.; Wu, L.; Liu, H. Gold Nanoparticles Dotted Reduction Graphene Oxide Nanocomposite Based Electrochemical Aptasensor for Selective, Rapid, Sensitive and Congener-Specific PCB77 Detection. *Sci. Rep.* **2017**, *7* (1), 1–7. https://doi.org/10.1038/s41598-017-05352-7.

(38) Lu, G.; Li, S.; Guo, Z.; Farha, O. K.; Hauser, B. G.; Qi, X.; Wang, Y.; Wang, X.; Han, S.; Liu, X.; Duchene, J. S.; Zhang, H.; Zhang, Q.; Chen, X.; Ma, J.; Loo, S. C. J.; Wei, W. D.; Yang, Y.; Hupp, J. T.; Huo, F. Imparting Functionality to a Metal-Organic Framework Material by Controlled Nanoparticle Encapsulation. *Nat. Chem.* **2012**, *4* (4), 310–316. https://doi.org/10.1038/nchem.1272.

(39) Kresse, G.; Hafner, J. Ab Initio Molecular-Dynamics Simulation of the Liquid-Metalamorphous- Semiconductor Transition in Germanium. *Phys. Rev. B* **1994**, *49* (20),

14251–14269. https://doi.org/10.1103/PhysRevB.49.14251.

(40) Kresse, G.; Hafner, J. Ab Initio Molecular Dynamics for Liquid Metals. *Phys. Rev. B* **1993**, *47* (1), 558–561. https://doi.org/10.1103/PhysRevB.47.558.

(41) Kresse, G.; Furthmüller, J. Efficiency of Ab-Initio Total Energy Calculations for Metals and Semiconductors Using a Plane-Wave Basis Set. *Comput. Mater. Sci.* **1996**, *6* (1), 15–50. https://doi.org/10.1016/0927-0256(96)00008-0.

(42) Kresse, G.; Furthmuller, J. Efficient Iterative Schemes for Ab Initio Total-Energy Calculations Using a Plane-Wave Basis Set. *Phys. Rev. B* **1996**, *54* (16), 11169–11186. https://doi.org/10.1021/acs.jpca.0c01375.

(43) Grimme, S.; Antony, J.; Ehrlich, S.; Krieg, H. A Consistent and Accurate Ab Initio Parametrization of Density Functional Dispersion Correction (DFT-D) for the 94 Elements H-Pu. *J. Chem. Phys.* **2010**, *132* (15). https://doi.org/10.1063/1.3382344.

(44) Stefan, G.; Stephan, E.; Goerigk, L. Effect of the Damping Function in Dispersion Corrected Density Functional Theory. *J. Comput. Chem.* **2012**, *32* (Sfb 858), 174–182. https://doi.org/10.1002/jcc.

(45) Jensen, S.; Tan, K.; Lustig, W.; Kilin, D.; Li, J.; Chabal, Y. J.; Thonhauser, T. Quenching of Photoluminescence in a Zn-MOF Sensor by Nitroaromatic Molecules. *J. Mater. Chem. C* **2019**, *7* (9), 2625–2632. https://doi.org/10.1039/c8tc06281a.

(46) Alahakoon, S. B.; Tan, K.; Pandey, H.; Diwakara, S. D.; McCandless, G. T.; Grinffiel, D. I.; Durand-Silva, A.; Thonhauser, T.; Smaldone, R. A. 2D-Covalent Organic Frameworks with Interlayer Hydrogen Bonding Oriented through Designed Nonplanarity. *J. Am. Chem. Soc.* **2020**, *142* (30), 12987–12994. https://doi.org/10.1021/jacs.0c03409.

(47) Silvi, B.; Savin, A. Classification of Chemical Bonds Based on Topological. *Nature* **1994**,

371 (6499), 683–686.

(48) De Silva, P.; Korchowiec, J.; Wesolowski, T. A. Revealing the Bonding Pattern from the Molecular Electron Density Using Single Exponential Decay Detector: An Orbital-Free Alternative to the Electron Localization Function. *ChemPhysChem* **2012**, *13* (15), 3462–3465. https://doi.org/10.1002/cphc.201200500.

(49) Chaplin, M. A Proposal for the Structuring of Water. *Biophys. Chem.* **1999**, *83* (November), 211**.**221. https://doi.org/10.1016/S0301-4622(99)00142-8.

(50) Auer, B.; Kumar, R.; Schmidt, J. R.; Skinner, J. L. Hydrogen Bonding and Raman, IR, and 2D-IR Spectroscopy of Dilute HOD in Liquid D2O. *Proc. Natl. Acad. Sci. U. S. A.* **2007**, *104* (36), 14215–14220. https://doi.org/10.1073/pnas.0701482104.

(51) Hu, Q.; Ouyang, S.; Li, J.; Cao, Z. Raman Spectroscopic Investigation on Pure D2O/H2O from 303 to 573 K: Interpretation and Implications for Water Structure. *J. Raman Spectrosc.* **2017**, *48* (4), 610–617. https://doi.org/10.1002/jrs.5088.

(52) Saraf, M.; Natarajan, K.; Mobin, S. M. Non-Enzymatic Amperometric Sensing of Glucose by Employing Sucrose Templated Microspheres of Copper Oxide (CuO). *Dalt. Trans.* **2016**, *45* (13), 5833–5840. https://doi.org/10.1039/c6dt00670a.

(53) Wu, L.; Fu, X.; Liu, H.; Li, J.; Song, Y. Comparative Study of Graphene Nanosheet- and Multiwall Carbon Nanotube-Based Electrochemical Sensor for the Sensitive Detection of Cadmium. *Anal. Chim. Acta* **2014**, *851* (C), 43–48. https://doi.org/10.1016/j.aca.2014.08.021.

(54) Zhai, D.; Liu, B.; Shi, Y.; Pan, L.; Wang, Y.; Li, W.; Zhang, R.; Yu, G. Highly Sensitive Glucose Sensor Based on Pt Nanoparticle/Polyaniline Hydrogel Heterostructures. *ACS Nano* **2013**, *7* (4), 3540–3546. https://doi.org/10.1021/nn400482d.

(55) Zhang, L.; Zhou, C.; Luo, J.; Long, Y.; Wang, C.; Yu, T.; Xiao, D. A Polyaniline Microtube

Platform for Direct Electron Transfer of Glucose Oxidase and Biosensing Applications. *J. Mater. Chem. B* **2015**, *3* (6), 1116–1124. https://doi.org/10.1039/c4tb01604a.

(56) Wen, Y.; Meng, W.; Li, C.; Dai, L.; He, Z.; Wang, L.; Li, M.; Zhu, J. Enhanced Glucose Sensing Based on a Novel Composite Co II -MOF/Acb Modified Electrode. *Dalt. Trans.* **2018**, *47* (11), 3872–3879. https://doi.org/10.1039/c8dt00296g.

(57) Shu, Y.; Yan, Y.; Chen, J.; Xu, Q.; Pang, H.; Hu, X. Ni and NiO Nanoparticles Decorated Metal-Organic Framework Nanosheets: Facile Synthesis and High-Performance Nonenzymatic Glucose Detection in Human Serum. *ACS Appl. Mater. Interfaces* **2017**, *9* (27), 22342–22349. https://doi.org/10.1021/acsami.7b07501.

(58) Xiao, X.; Zheng, S.; Li, X.; Zhang, G.; Guo, X.; Xue, H.; Pang, H. Facile Synthesis of Ultrathin Ni-MOF Nanobelts for High-Efficiency Determination of Glucose in Human Serum. *J. Mater. Chem. B* **2017**, *5* (26), 5234–5239. https://doi.org/10.1039/c7tb00180k.

(59) Wang, L.; Ling, Y.; Han, L.; Zhou, J.; Sun, Z.; Li, N. B.; Luo, H. Q. Catalase Active Metal-Organic Framework Synthesized by Ligand Regulation for the Dual Detection of Glucose and Cysteine. *Anal. Chim. Acta* **2020**, *1131*, 118–125. https://doi.org/10.1016/j.aca.2020.07.051.

(60) Abrori, S. A.; Septiani, N. L. W.; Hakim, F. N.; Maulana, A.; Suyatman; Nugraha; Anshori, I.; Yuliarto, B. Non-Enzymatic Electrochemical Detection for Uric Acid Based on a Glassy Carbon Electrode Modified with MOF-71. *IEEE Sens. J.* **2021**, *21* (1), 170–177. https://doi.org/10.1109/JSEN.2020.3014298.

(61) Gumilar, G.; Kaneti, Y. V.; Henzie, J.; Chatterjee, S.; Na, J.; Yuliarto, B.; Nugraha, N.; Patah, A.; Bhaumik, A.; Yamauchi, Y. General Synthesis of Hierarchical Sheet/Plate-like M-BDC (M = Cu, Mn, Ni, and Zr) Metal-Organic Frameworks for Electrochemical Non-

Enzymatic Glucose Sensing. *Chem. Sci.* **2020**, *11* (14), 3644–3655. https://doi.org/10.1039/c9sc05636j.

(62) Chen, Q.; Chu, D.; Yan, L.; Lai, H.; Chu, X.-Q.; Ge, D.; Chen, X. Enhanced Non-Enzymatic Glucose Sensing Based on Porous ZIF-67 Hollow Nanoprisms. *New J. Chem.* **2021**, 10031–10039. https://doi.org/10.1039/d1nj01138c.

(63) Hu, S.; Lin, Y.; Teng, J.; Wong, W. L.; Qiu, B. In Situ Deposition of MOF-74(Cu) Nanosheet Arrays onto Carbon Cloth to Fabricate a Sensitive and Selective Electrocatalytic Biosensor and Its Application for the Determination of Glucose in Human Serum. *Microchim. Acta* **2020**, *187* (12). https://doi.org/10.1007/s00604-020-04634-8.

(64) Zhou, Y.; Hu, Q.; Yu, F.; Ran, G. Y.; Wang, H. Y.; Shepherd, N. D.; D'Alessandro, D. M.; Kurmoo, M.; Zuo, J. L. A Metal-Organic Framework Based on a Nickel Bis(Dithiolene) Connector: Synthesis, Crystal Structure, and Application as an Electrochemical Glucose Sensor. *J. Am. Chem. Soc.* **2020**, *142* (48), 20313–20317. https://doi.org/10.1021/jacs.0c09009.

(65) Hrapovic, S.; Liu, Y.; Male, K. B.; Luong, J. H. T. Platinum Nanoparticles and Carbon Nanotubes Interactions with Pt Nanoparticles to Form a Network That Connected Pt Nanoparticles to the Electrode Surface . TEM Nanoparticles on Carbon Nanotubes Whereas Cyclic Volta-. **2004**, *76* (4), 1083–1088. https://doi.org/10.1021/ac035143t.

(66) Park, S.; Boo, H.; Dong, T. Electrochemical Non-Enzymatic Glucose Sensors. **2006**, *556*, 46–57. https://doi.org/10.1016/j.aca.2005.05.080.

(67) da Silva, R. P.; Lima, A. W. O.; Serrano, S. H. P. Simultaneous Voltammetric Detection of Ascorbic Acid, Dopamine and Uric Acid Using a Pyrolytic Graphite Electrode Modified into Dopamine Solution. *Anal. Chim. Acta* **2008**, *612* (1), 89–98.

https://doi.org/10.1016/j.aca.2008.02.017.

(68) Zhang, Y.; Pan, H.; Murugananthan, M.; Sun, P.; Dionysiou, D. D.; Zhang, K.; Khan, A.; Zhang, Y. Glucose and Melamine Derived Nitrogen-Doped Carbonaceous Catalyst for Nonradical Peroxymonosulfate Activation Process. *Carbon N. Y.* **2020**, *156*, 399–409. https://doi.org/10.1016/j.carbon.2019.09.050.

(69) Zhang, X.; Zhao, H.; Xue, Y.; Wu, Z.; Zhang, Y.; He, Y.; Li, X.; Yuan, Z. Colorimetric Sensing of Clenbuterol Using Gold Nanoparticles in the Presence of Melamine. *Biosens. Bioelectron.* **2012**, *34* (1), 112–117. https://doi.org/10.1016/j.bios.2012.01.026.

(70) Ma, Z.; Zhang, H.; Yang, Z.; Ji, G.; Yu, B.; Liu, X.; Liu, Z. Mesoporous Nitrogen-Doped Carbons with High Nitrogen Contents and Ultrahigh Surface Areas: Synthesis and Applications in Catalysis. *Green Chem.* **2016**, *18* (7), 1976–1982. https://doi.org/10.1039/c5gc01920f.

Supporting Information for

Hydrogen-Bonding 2D Coordination Polymer for Enzyme-Free Electrochemical Glucose Sensing

*Xiaochen Fu,[a] Matthew Sale,[a] Bowen Ding,[a] William Lewis,[b] Debbie Silvester-Dean,[c] Chris D. Ling,[a] Deanna M. D'Alessandro[a]**

a School of Chemistry, The University of Sydney, Sydney, New South Wales 2006, Australia

b Sydney Analytical, Core Research Facilities, The University of Sydney, Sydney, New South Wales 2006, Australia

c School of Molecular and Life Sciences, Curtin University, GPOBox U1987, Perth 6845, Western Australia, Australia

*Corresponding Author: deanna.dalessandro@sydney.edu.au, phone +61 2 9351 3777, fax: +61 3 9351 3329

Contents

1 General Methods and Instrumentation

All starting materials were purchased from Sigma Aldrich and were used as received without further purification. The solvents were reagent grade.

1.1. Powder X-ray Diffraction (PXRD): PXRDs

Powder X-ray diffraction (PXRD) patterns were recorded with a PANalytical X'Pert MPD (Cu Kα, λ=1.5418 Å) within the 2θ range 5-50° at room temperature.

1.2. Thermogravimetric analysis (TGA)

Thermogravimetric analysis (TGA) was carried out in a nitrogen stream using Hiden-Isochema IGA-002 gravimetric equipment with heating from room temperature up to 700 ℃ at a heating rate of 10 ℃·min^{-1}.

1.3. Electrochemistry

The electrochemical performance was measured with a Bioanalytical Systems (BASi) Potentiostat for cyclic voltammetry (CV) and differential pulse voltammetry (DPV). CV and DPV measurements were performed in 0.1 mM $K_3[Fe(CN)_6]/K_4[Fe(CN)_6]$ (1:1) solution containing 0.5 mM KCl at a scan rate of 100 mV/s (for CV) scanning the potential from 0 V to +0.5 V and back to 0 V. The parameters for DPV were: pulse width 50 ms, pulse period 200 ms, pulse amplitude 50 mV and step E 4 mV, scanning the potential from 0 V to 0.5 V . All experiments were carried out at room temperature with a three-electrode system. The glassy carbon electrode (GC) (3.0 mm diameter) was used as the working electrode, a Ag/AgCl electrode (3 M KCl) as a reference electrode, and a platinum wire (0.1

mm wire diameter) as the auxiliary electrode (all electrodes were purchased from BASi USA).

1.4. Raman Spectroscopy and VT Raman Spectroscopy

Raman spectra were collected using an inVia Renishaw Raman Spectrometer with 785 nm laser excitation (Argon ion). In situ variable temperature Raman (VT- Raman spectra) were collected using Linkam stage, temperature points from 25 to 50, 75, 100, 125, 150, 175, 200, 225, 250 ºC with a rate of ~7 ºC /min. All the samples were sealed in glass capillary (diameter 1 mm).

1.5. Electrochemical Sensing and Fabrication of modified GC Electrodes.

The ground CP1 (10 mg) was dispersed in DMF (1 mL) to achieve a 10 mg/mL suspension and was sonicated for 5 minutes to form a homogeneous dispersion. The GC electrode (3 mm diameter) was polished with 0.3 um Al_2O_3 slurry for 5 minutes, then sonicated in ethanol/water (1:1, v/v) solution for 1 minute, repeat for 3 times. 10 μL of the suspension was drop-casted onto the surface of the GCE overnight and left to dry in air.

2 Synthesis

2.1. Synthesis of $[Zn_2(BPDC)_1Mel_{0.5}\text{-}Mel_{0.5}]\cdot(DMF_{0.6})$ {denoted CP1}.

$Zn(CH_3COO)_2\cdot 2H_2O$(0.4 mM, 87.8 mg), 1,3,5-triazine-2,4,6-triamine (0.4 mM, 47.3 mg) and biphenyl-4,4′-dicarboxylic (0.6 mM, 145.3 mg) were added to a mixture of DMF and MeOH (in a ratio of 4:1=v/v, 10 ml) before the addition of 1% H_2O. The mixture was heated in the oven to 90 °C for 72 hours. The solution was cooled down to room temperature and the yellow hexagonal crystals were collected and sorted in DMF. Anal. Calcd (%) for $[Zn_2(BPDC)_1Mel_{0.5}\text{-}Mel_{0.5}]\cdot(DMF_{0.6})$ C, 44.236; N, 18.061; H, 4.641. Found (%): C, 47.010; N, 12.200; H, 3.587. The difference between the predicted and calculated elemental analysis results is not uncommon for CPs and reflects the porous nature of the materials that are susceptible to adsorption and desorption of guests (S.I. Figure. S2). Crystal structure data can be obtained from the Cambridge Crystallographic Data Center (CCDC 2036487).

2.2. Synthesis of Gold Nanoparticles (AuNPs).

The AuNPs were synthesized according to the literature procedure with no modifications.1 According to the literature, the size of the nanoparticles was 20 nm.

2.3. Synthesis of Platinum Nanoparticles (PtNPs).

The PtNPs were synthesized according to the literature procedure with no modifications.[2] According to the literature, the size of the nanoparticles was 4.1 nm.

3 Crystal Structure

3.1. Single Crystal X-Ray Diffraction

Table S1. Crystallographic parameters (CCDC 2036487)

Empirical formula	$C_{20}H_{22}N_{12}O_4Zn$
Formula weight	559.86
Temperature/K	100.01(10)
Crystal system	orthorhombic
Space group	Abm2
a/Å	17.5983(4)
b/Å	24.5934(3)
c/Å	18.2648(2)
α/°	90
β/°	90
γ/°	90
Volume/Å^3	7905.0(2)
Z	12
ρ_{calc}g/cm^3	1.411
μ/mm^{-1}	1.730
F(000)	3456.0
Radiation	CuKα (λ = 1.54178)
2Θ range for data collection/°	7.188 to 145.164
Index ranges	$-21 \leq h \leq 13$, $-18 \leq k \leq 30$, $-22 \leq l \leq 22$
Reflections collected	16740
Independent reflections	7498 [R_{int} = 0.0244, R_{sigma} = 0.0310]
Data/restraints/parameters	7498/1/342
Goodness-of-fit on F^2	1.036
Final R indexes [I>=2σ (I)]	R_1 = 0.0461, wR_2 = 0.1255
Final R indexes [all data]	R_1 = 0.0482, wR_2 = 0.1271
Largest diff. peak/hole / e Å^{-3}	0.82/-0.53
Flack parameter	0.28(2)

a

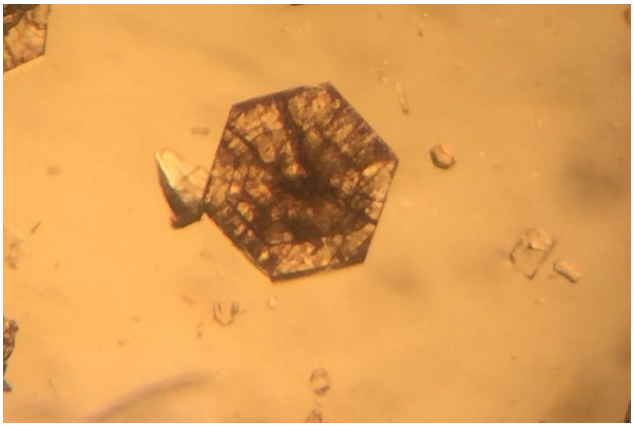

b

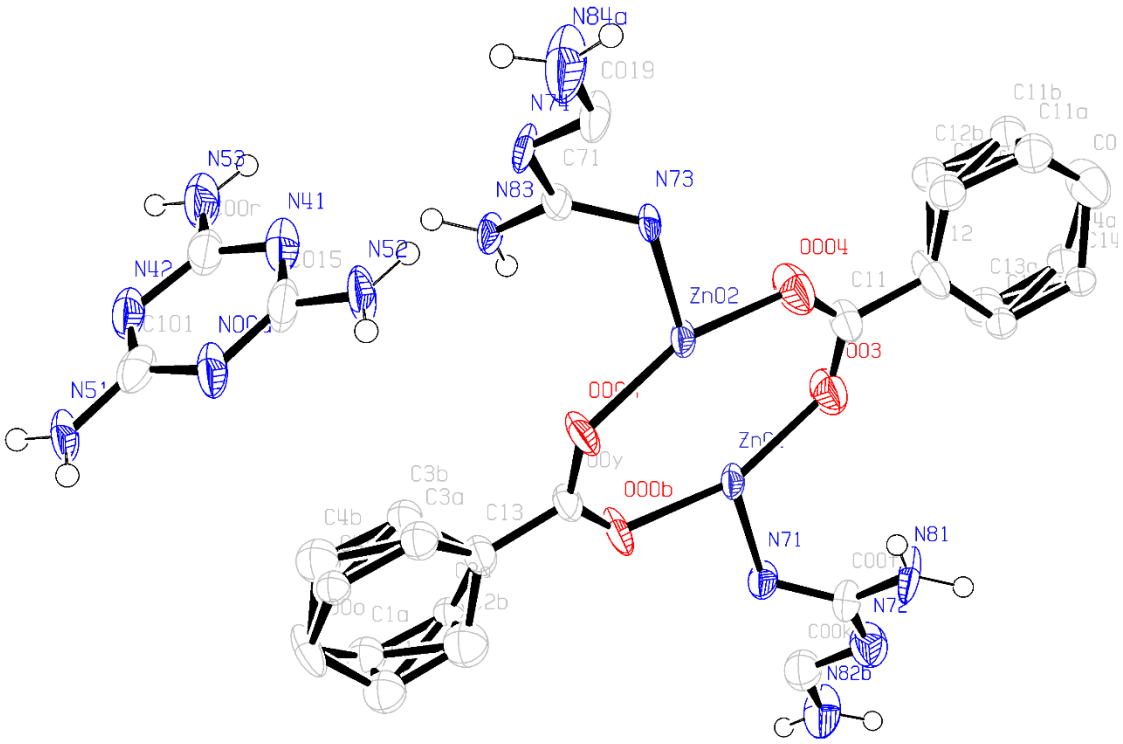

Figure S1. (a) Image of the unit cell of CP1; (b) ORTEP diagram of CP1.

3.2. Powder X-Ray Diffraction

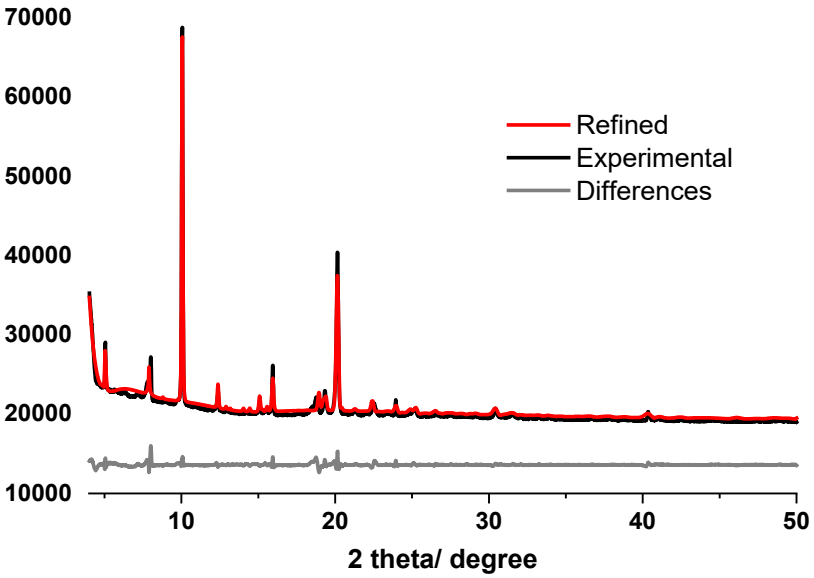

Figure S2. The refined PXRD of CP1 pattern in red), the experimental PXRD pattern for CP1 in black) and the differences plot in gray.

The comparation of the simulated and experimental PXRD patterns are shown in Figure S2. The close correspondences of peak positions illustrate the structure is correct. The blue (refined) plot of Figure S2 indicates an acceptable fitted degree with R_p = 6.648%, wR_P = 10.307%, where the R_p and wR_P are agreement factors.

Due to the favorable coordination between Zn(II) and carboxylate-based ligands, the IRMOF-10 2D sheet structure (CCDC 186896) was initially considered as a structural component. To further confirm we incorporated melamine into the crystal structure, we compared the PXRD of pure [Zn(BPDC)] (IRMOF-10) with that of our CP. We found that IRMOF-10 decomposed in H_2O immediately, but the chemical stability of our CP (i.e. stability under aqueous conditions) has been significantly enhanced by incorporating melamine into the framework. We envisage that the H-bonding within the framework may contribute to the enhanced stability.

4 Thermogravimetric analysis (TGA)

The thermogravimetric analysis (TGA) curve shows a weight loss of 25% from 25 to 250 °C, which could be attributed to the loss of the DMF, MeOH and coordinated DMF molecules in the molecular unit. After a plateau until 370 °C, the samples begin to decompose with complete collapse at 550 °C.

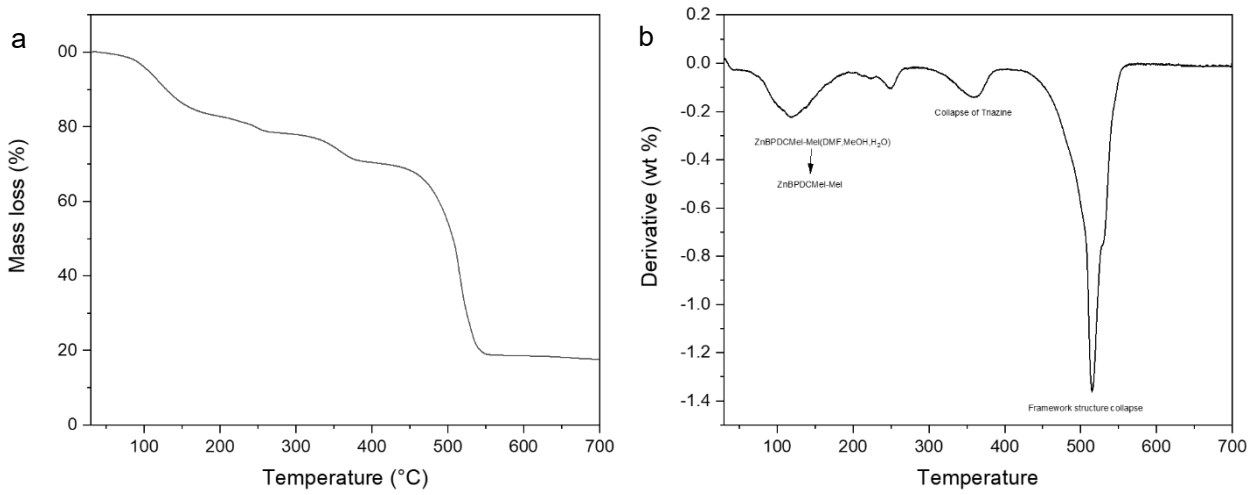

Figure S3. (a) The TGA of CP1 (under N_2, up to 700 °C) shows a multi-step decomposition. The 1st decrease between 20-250 could be the solvent (MeOH and H_2O) loss before 250 °C; then the 2nd step which is in the range between 250-350 °C due to the loss of DMF molecule[3]; the 3rd step could be the collapse of the melamine structure[4]; and the significant 4th weight loss over the range370-550 °C could due to framework collapse. (b) DTG of CP1.

5 Raman spectrum analysis

Raman spectra were collected using an inVia Renishaw Raman Spectrometer with 785 nm laser excitation (Argon ion). In situ variable temperature Raman (VT- Raman spectra) were collected using a Linkam stage, with temperature points at 25, 50, 75, 100, 125, 150, 175, 200, 225, 250 ºC with a heating rate of ~7 ºC /min. All of the samples were sealed in glass capillaries (diameter 1 mm).

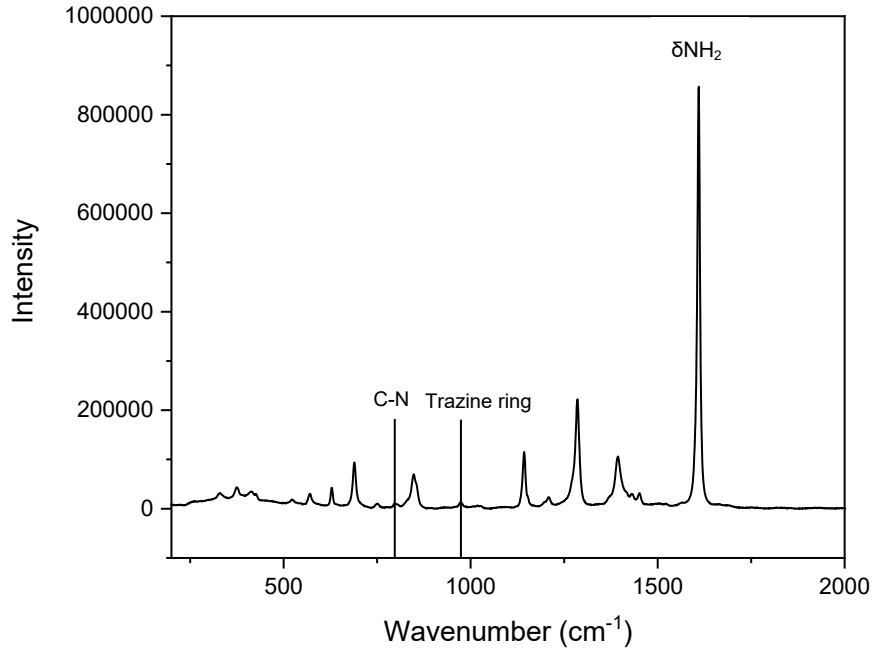

Figure S4. Raman spectrum of CP1 at room temperature

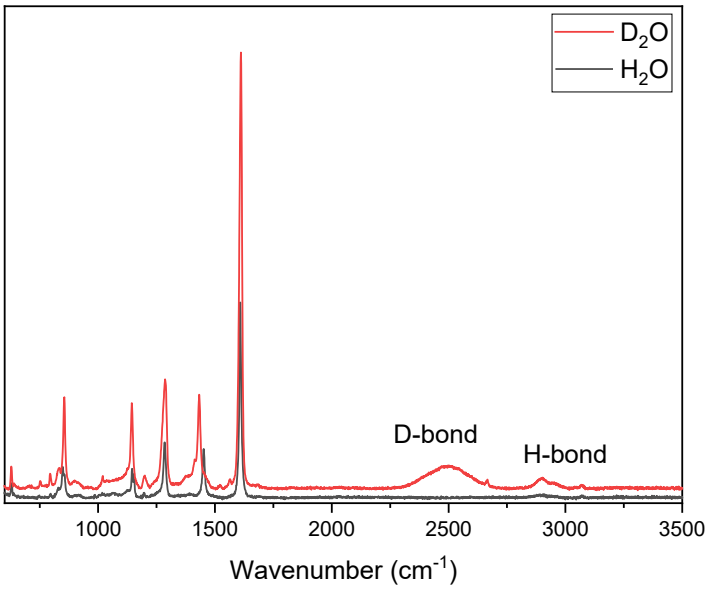

Figure S5. Raman Comparation of CP1 in D_2O and H_2O glucose solution at room temprature

6 Computational studies of CP1

Density functional theory (DFT) calculations[3–6] were performed with VASP 5.4.4 including Van der Walls dispersion corrections using the D3 and Becke-Jonson approximation [DFT-D3(BJ)] [7,8] to represent hydrogen bonding. The generalized gradient approximation of Perdew, Burke and Ernzerhof (PBE)[11] with the projector augmented-wave (PAW) method was used.[12,13] The plane-wave energy cut-off was set to 410 eV and the energy convergence criteria was 10^{-6} eV. A single k-point at the gamma point[9] was employed with the Gaussian smearing method[10] and a sigma value of 0.05. The CP structure consisted of the as obtained from the single crystal experiment as in Figure S1b and also Figure 4a; two sets of alternating Zn(BPDC)Mel 2D net work and interstitial melamine layers with hydrogen termination where necessary were selected in Olex2 (Figure 3a in main text).

Since the framework contains Zn, the commonly used Hubbard U-J correction was employed.[16] A value for U-J of 16.2 eV was determined using the variational linear response approach method of Cococcioni.[17] This value is significantly higher than other commonly used values found in the literature of 7.5 eV and 12 eV,[18–21] which is consistent with literature which predicts the difficulty of using this method for determining U-J for atomic species with fully filled electron shells.[22] As a result, all calculations were repeated with a range of U-J values of from 0 eV to 16 eV in 2 eV steps with a few extra U-V values. We found little effect on the final calculated quantities as shown in Figure S9 and as a result, we used the value of U-J of 16.2 eV for the results presented in the main text. Specifically, the relaxed geometries and ELF results were very similar as in Figures S8 and S9.

The Geometry optimizations were performed to reduce the Pulay stress.[23] This method is similar to the relaxation scheme used for other CP/MOFs.[24] This resulted in a structure where the positions were optimized until all forces between atoms were smaller than 1 meV/Å.

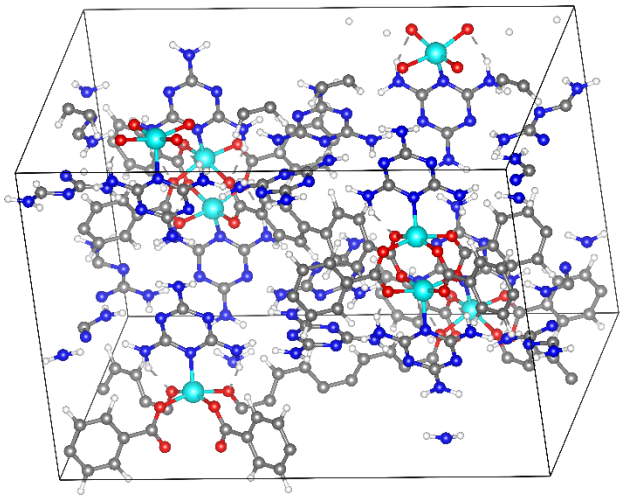

Figure S6 CP1 backbone in a 1 × 1 × 1 supercell with U = 16.2 eV. grey = carbon, red = oxygen, light blue = zinc, blue = nitrogen.

6.1 Unit cell parameters as a function of U-J

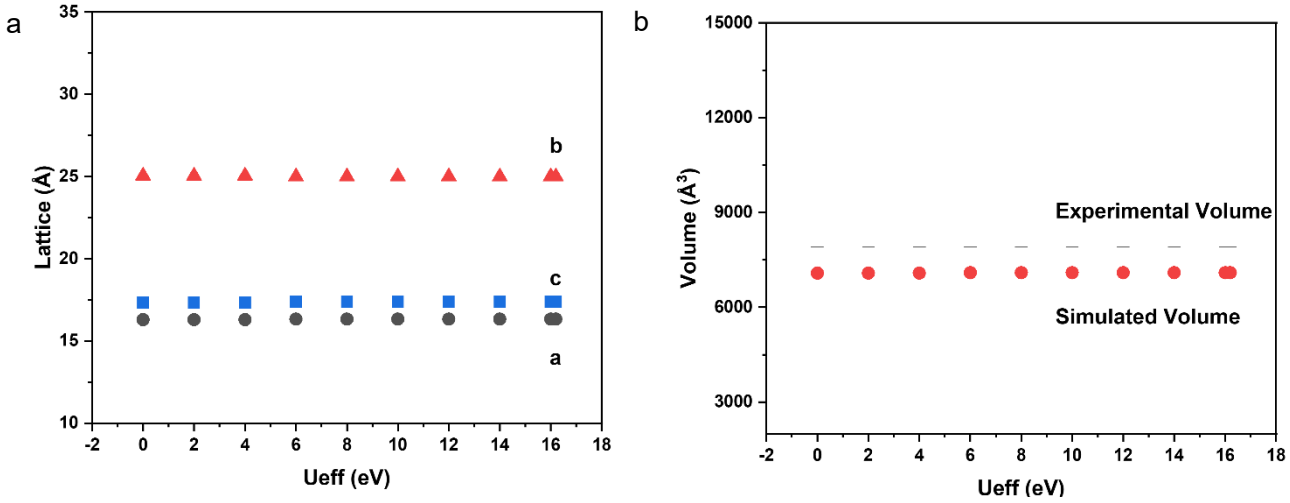

Figure S7 The lattice parameter (a) and volume of unit cell (b) in different U values. The experimental unit cell volume value is shown by the dashed lines (b).

6.2 Geometry optimization with different U values

U = 0

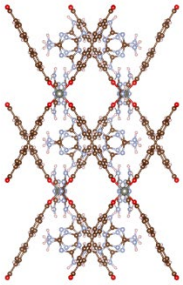

U = 6

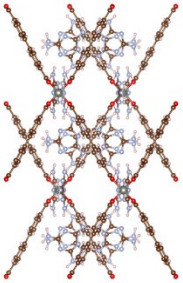

U = 2

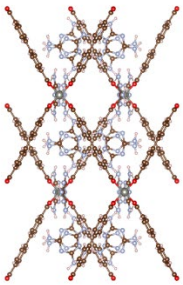

U = 8

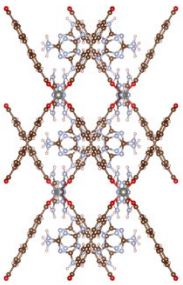

U = 4

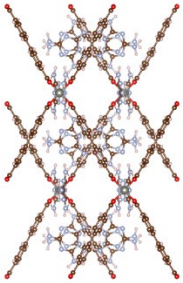

U = 10

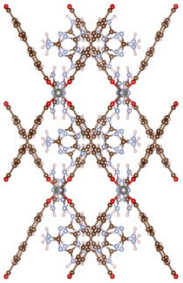

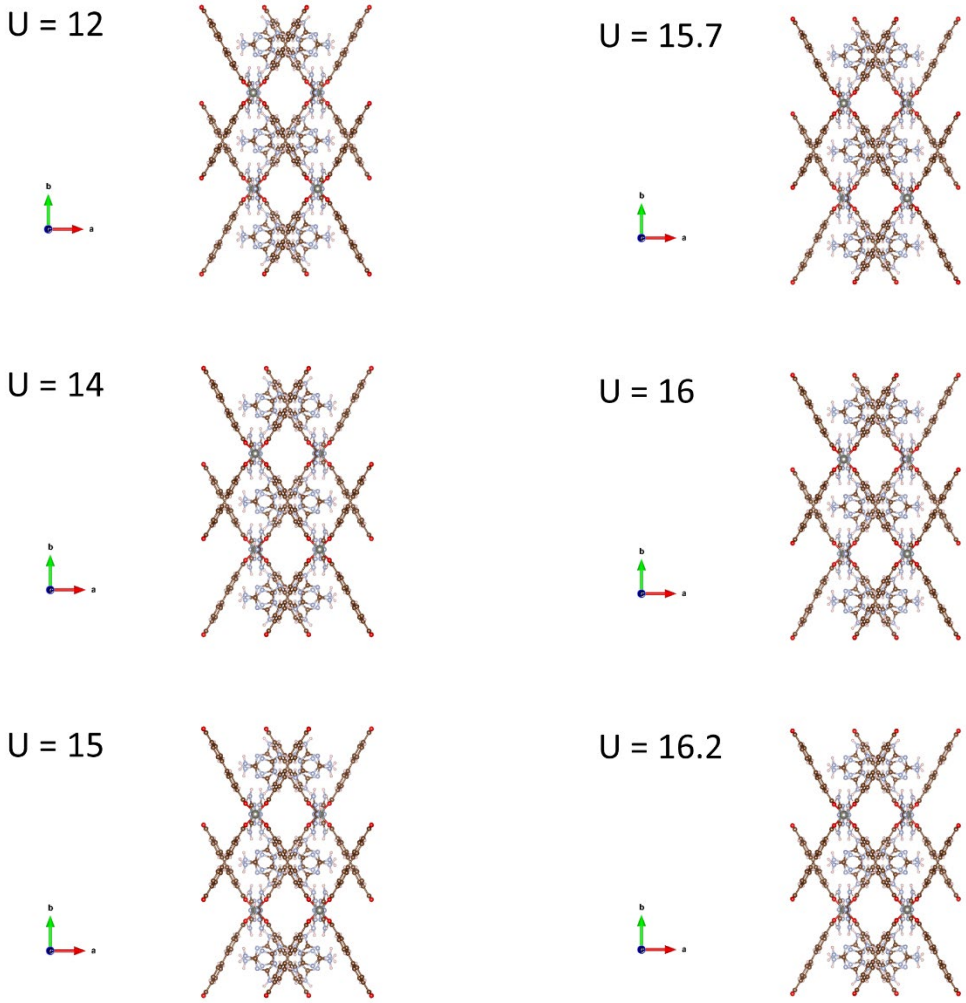

Figure S8. Geometry Optimization with different U values in the Zn based system (strong corelated system) (U=0, 2, 4, 6, 8, 10, 12, 14 , 15, 15.7, 16, 16.2).

6.3 Electron localization function (ELF) optimization with different U values

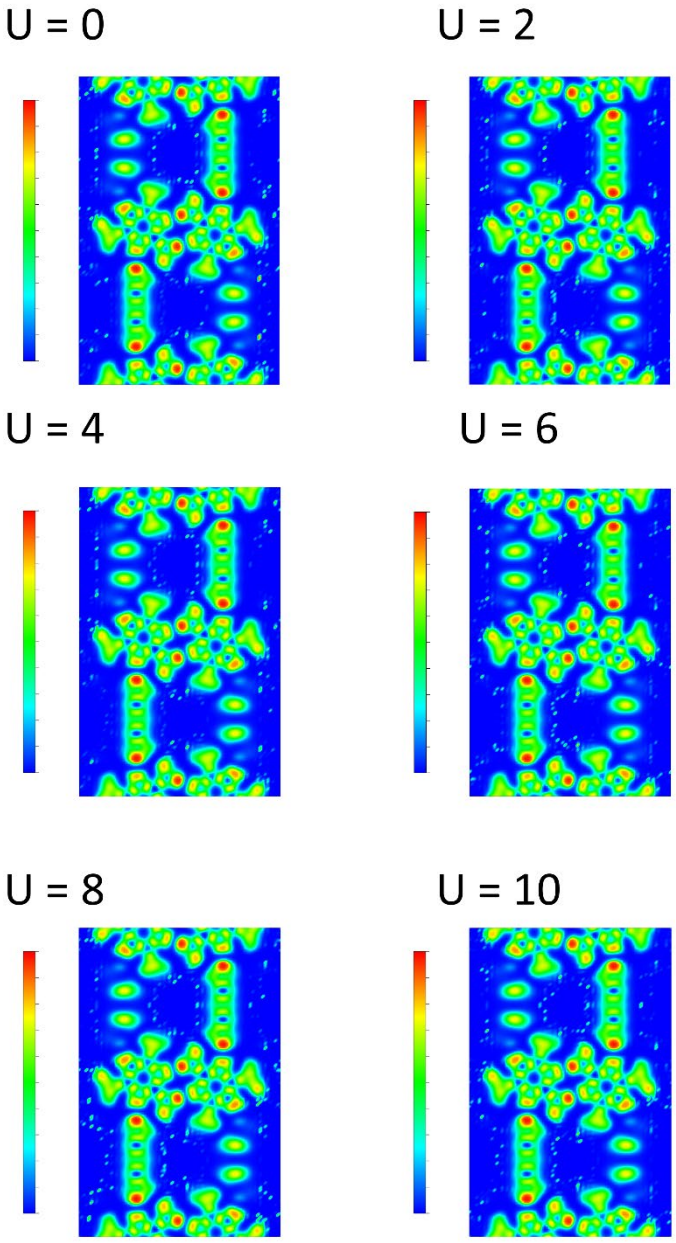

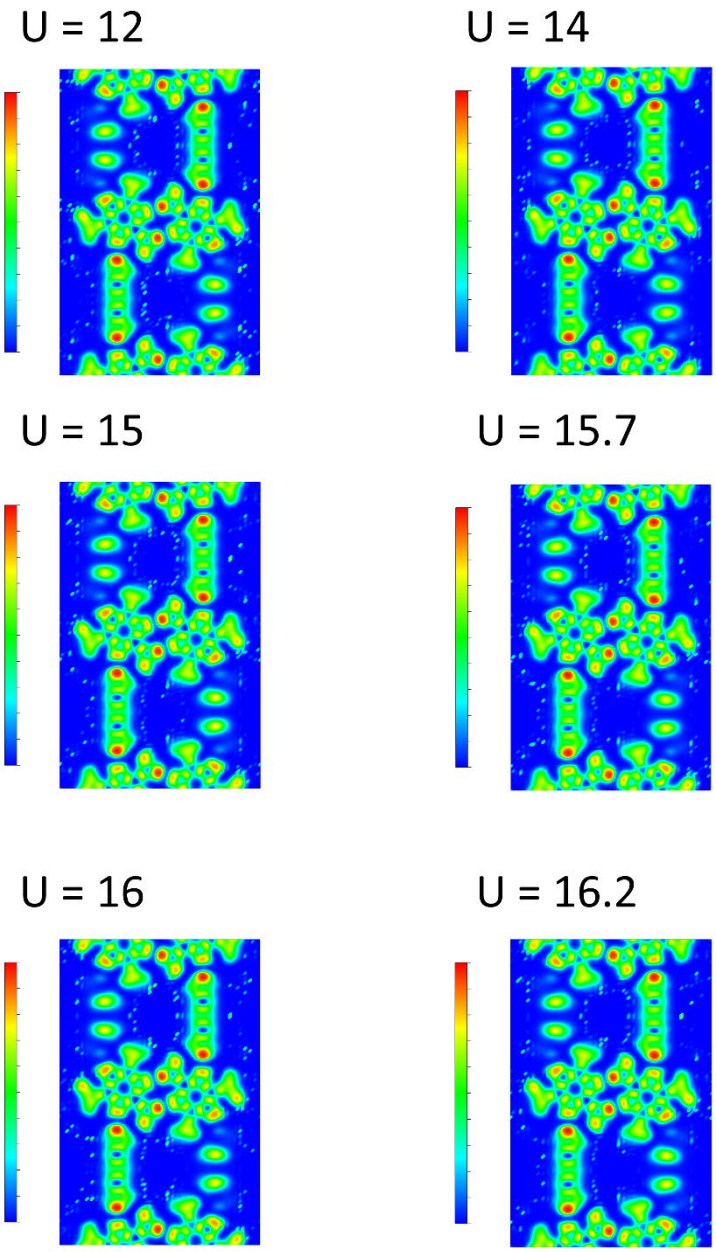

Figure S9. Optimization of ELF 2d cut plane at face 0,0,1 for different U values for the Zn based system (strong corelated system) (U=0, 4, 6, 8, 10, 12, 15, 15.7, 16, 16.2).

6.4 Table of bond distances

Table S1 Comparation of experimental and simulated Hydrogen bond lengths

Bonding Source Molecule		Bonding Name	Experimental Bond length (Å)	Simulated Bond length (Å)	Differences %
Interstitial Melamine 1		H68···N20	2.22881	1.94044	12.93829443
		N72···H4	2.24942	2.01619	10.36845053
		N80···H24	2.19909	2.06804	5.959283158
	Interstitial Melamine 2	H52···N27	2.15107	1.78657	16.94505525
		N28···H51	2.15107	1.78786	16.8850851
		N79···H23	2.19909	2.06782	5.969287296
		N71···H3	2.24942	2.01526	10.40979452
		H67···N19	2.22881	1.94037	12.94143512

7 ELECTROCHEMICAL SENSING

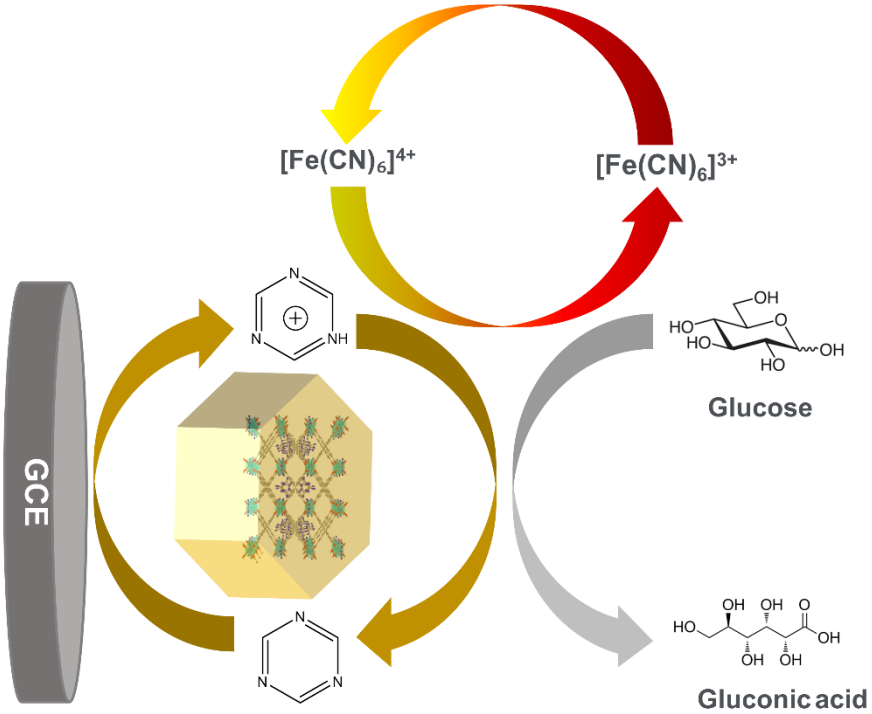

Figure S10. Schematic illustration of the sensing mechanism of CP1/GCE for glucose oxidation electron transfer.

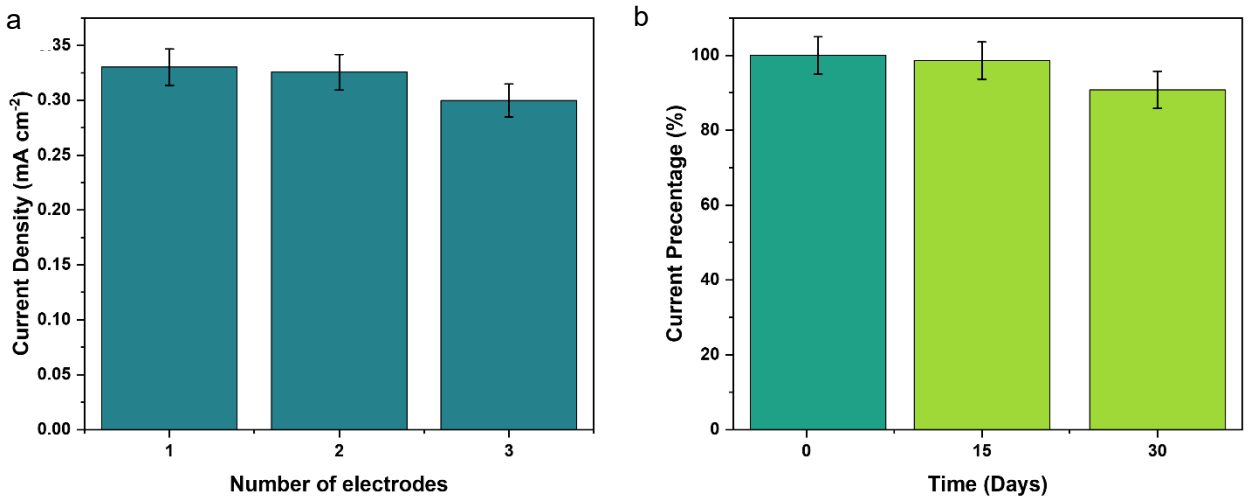

Figure S11. (a) Current densities of CP1/GC to 5 mM glucose for testing of 3 individual CP1/GC electrodes. The error bars denote the standard deviations. (b) Stability of CP1/GC to 5 mM glucose with 15 days measurement over 1 month. The error bars denote the standard deviations.

8 References

(1) Wu, L.; Lu, X.; Fu, X.; Wu, L.; Liu, H. Gold Nanoparticles Dotted Reduction Graphene Oxide Nanocomposite Based Electrochemical Aptasensor for Selective, Rapid, Sensitive and Congener-Specific PCB77 Detection. *Sci. Rep.* **2017**, *7* (1), 1–7. https://doi.org/10.1038/s41598-017-05352-7.

(2) Lu, G.; Li, S.; Guo, Z.; Farha, O. K.; Hauser, B. G.; Qi, X.; Wang, Y.; Wang, X.; Han, S.; Liu, X.; Duchene, J. S.; Zhang, H.; Zhang, Q.; Chen, X.; Ma, J.; Loo, S. C. J.; Wei, W. D.; Yang, Y.; Hupp, J. T.; Huo, F. Imparting Functionality to a Metal-Organic Framework Material by Controlled Nanoparticle Encapsulation. *Nat. Chem.* **2012**, *4* (4), 310–316. https://doi.org/10.1038/nchem.1272.

(3) Sahiner, N.; Demirci, S.; Sel, K. Covalent Organic Framework Based on Melamine and Dibromoalkanes for Versatile Use. *J. Porous Mater.* **2016**, *23* (4), 1025–1035. https://doi.org/10.1007/s10934-016-0160-9.

(4) Yin, N.; Wang, K.; Xia, Y.; Li, Z. Novel Melamine Modified Metal-Organic Frameworks for Remarkably High Removal of Heavy Metal Pb (II). *Desalination* **2018**, *430* (July 2017), 120–127. https://doi.org/10.1016/j.desal.2017.12.057.

(5) Kresse, G.; Hafner, J. Ab Initio Molecular-Dynamics Simulation of the Liquid-Metalamorphous- Semiconductor Transition in Germanium. *Phys. Rev. B* **1994**, *49* (20), 14251–14269. https://doi.org/10.1103/PhysRevB.49.14251.

(6) Kresse, G.; Hafner, J. Ab Initio Molecular Dynamics for Liquid Metals. *Phys. Rev. B* **1993**, *47* (1), 558–561. https://doi.org/10.1103/PhysRevB.47.558.

(7) Kresse, G.; Furthmüller, J. Efficiency of Ab-Initio Total Energy Calculations for Metals and Semiconductors Using a Plane-Wave Basis Set. *Comput. Mater. Sci.* **1996**, *6* (1), 15–50. https://doi.org/10.1016/0927-0256(96)00008-0.

(8) Kresse, G.; Furthmuller, J. Efficient Iterative Schemes for Ab Initio Total-Energy Calculations Using a Plane-Wave Basis Set. *Phys. Rev. B* **1996**, *54* (16), 11169–11186. https://doi.org/10.1021/acs.jpca.0c01375.

(9) Grimme, S.; Antony, J.; Ehrlich, S.; Krieg, H. A Consistent and Accurate Ab Initio Parametrization of Density Functional Dispersion Correction (DFT-D) for the 94 Elements H-Pu. *J. Chem. Phys.* **2010**, *132* (15). https://doi.org/10.1063/1.3382344.

(10) Stefan, G.; Stephan, E.; Goerigk, L. Effect of the Damping Function in Dispersion Corrected Density Functional Theory. *J. Comput. Chem.* **2012**, *32* (Sfb 858), 174–182. https://doi.org/10.1002/jcc.

(11) Hendrik J. Monkhorst and James D. Pack. Special Points for Brillonin-Zone Integrations*. *Phys. Rev. B* **1976**, *13* (12), 5188. https://doi.org/10.1039/c8ta11250a.

(12) Fu, C. L.; Ho, K. M. First-Principles Calculation of the Equilibrium Ground-State Properties of Transition Metals: Applications to Nb and Mo. *Phys. Rev. B* **1983**, *28* (10), 5480–5486. https://doi.org/10.1103/PhysRevB.28.5480.

(13) Perdew, J. P.; Burke, K.; Ernzerhof, M. Generalized Gradient Approximation Made Simple. *Phys. Rev. Lett.* **1996**, *77* (18), 3865–3868. https://doi.org/10.1103/PhysRevLett.77.3865.

(14) Blöchl, P. E. Projector Augmented-Wave Method. *Phys. Rev. B* **1994**, *50* (24), 17953–17979. https://doi.org/10.1103/PhysRevB.50.17953.

(15) Kresse, G. ; Joubert, D. From Ultrasoft Pseudopotentials to the Projector Augmented-Wave Method. *Phys. Rev. B - Condens. Matter Mater. Phys.* **1999**, *59* (3), 1758–1775.

https://doi.org/10.1103/PhysRevB.59.1758.
(16) Dudarev, S. L.; Botton, G. A.; Savrasov, S. Y.; Humphreys, C. J. and Sutton, A. P. Electron-Energy-Loss Spectra and the Structural Stability of Nickel Oxide: An LSDA+U Study. *Phys. Rev. B - Condens. Matter Mater. Phys.* **1998**, *57* (3), 1505–1509. https://doi.org/10.1103/PhysRevB.57.1505.
(17) Cococcioni, M.; De Gironcoli, S. Linear Response Approach to the Calculation of the Effective Interaction Parameters in the LDA+U Method. *Phys. Rev. B - Condens. Matter Mater. Phys.* **2005**, *71* (3), 1–16. https://doi.org/10.1103/PhysRevB.71.035105.
(18) Azar, Y. T.; Lakmehsari, M. S.; Kazem Manzoorolajdad, S. M.; Sokhanvaran, V.; Ahadi, Z.; Shahsavani, A.; Hopke, P. K. A DFT Screening of Magnetic Sensing-Based Adsorption of NO by M-MOF-74 (M= Mg, Ti, Fe and Zn). *Mater. Chem. Phys.* **2020**, *239* (April 2019), 122105. https://doi.org/10.1016/j.matchemphys.2019.122105.
(19) Zasada, F.; Piskorz, W.; Gryboś, J.; Sojka, Z. Periodic DFT+D Molecular Modeling of the Zn-MOF-5(100)/(110)TiO2 Interface: Electronic Structure, Chemical Bonding, Adhesion, and Strain. *J. Phys. Chem. C* **2014**, *118* (17), 8971–8981. https://doi.org/10.1021/jp412756a.
(20) Consiglio, A.; Tian, Z. Importance of the Hubbard Correction on the Thermal Conductivity Calculation of Strongly Correlated Materials: A Case Study of ZnO. *Sci. Rep.* **2016**, *6* (November), 1–7. https://doi.org/10.1038/srep36875.
(21) Goh, E. S.; Mah, J. W.; Yoon, T. L. Effects of Hubbard Term Correction on the Structural Parameters and Electronic Properties of Wurtzite ZnO. *Comput. Mater. Sci.* **2017**, *138*, 111–116. https://doi.org/10.1016/j.commatsci.2017.06.032.
(22) Yu, K.; Carter, E. A. Communication: Comparing Ab Initio Methods of Obtaining Effective U Parameters for Closed-Shell Materials. *J. Chem. Phys.* **2014**, *140* (12). https://doi.org/10.1063/1.4869718.
(23) Francis, G. P.; Payne, M. C. Finite Basis Set Corrections to Total Energy Pseudopotential Calculations. *J. Phys. Condens. Matter* **1990**, *2* (19), 4395–4404. https://doi.org/10.1088/0953-8984/2/19/007.
(24) Jensen, S.; Tan, K.; Lustig, W.; Kilin, D.; Li, J.; Chabal, Y. J.; Thonhauser, T. Quenching of Photoluminescence in a Zn-MOF Sensor by Nitroaromatic Molecules. *J. Mater. Chem. C* **2019**, *7* (9), 2625–2632. https://doi.org/10.1039/c8tc06281a.